Title

Decomposing Cloud Radiative Feedbacks by Cloud-Top Phase

Journal

Journal of Climate, 38(16)

ISSN

0894-8755

Authors

Wall, Casey J

Paynter, David

Qin, Yi

et al.

Publication Date

2025-08-15

DOI

10.1175/jcli-d-24-0538.1

Decomposing Cloud Radiative Feedbacks by Cloud-Top Phase

Casey J. Wall,[a,b] David Paynter,[c] Yi Qin,[d] Matvey Debolskiy,[e] Margaret L. Duffy,[f,g] Takuro Michibata,[h] Brandon M. Duran,[i] Nicholas J. Lutsko,[i] Po-Lun Ma,[d] Brian Medeiros,[f] Trude Storelvmo,[e,j] Ming Zhao[c]

[a] *Department of Meteorology, Stockholm University, Stockholm, Sweden*

[b] *Bolin Centre for Climate Research, Stockholm University, Stockholm, Sweden*

[c] *NOAA Geophysical Fluid Dynamics Laboratory, Princeton, NJ, USA*

[d] *Pacific Northwest National Laboratory, Richland, WA, USA*

[e] *Department of Geosciences, University of Oslo, Oslo, Norway*

[f] *NSF National Center for Atmospheric Research, Boulder, CO, USA*

[g] *Department of Earth and Planetary Sciences, University of California, Berkeley, CA, USA*

[h] *Research Institute for Applied Mechanics, Kyushu University, Fukuoka, Japan*

[i] *Scripps Institution of Oceanography, University of California San Diego, La Jolla, CA, USA*

[j] *Graduate School of Business, Nord University, Bodø, Norway*

Corresponding author: Casey J. Wall, casey.wall@misu.su.se

ABSTRACT

Changes in cloud scattering properties and emissivity that arise from atmospheric warming cause substantial radiative feedbacks in model projections of anthropogenic climate change, and the relative importance of the underlying mechanisms is poorly understood. One leading hypothesis is that ice-to-liquid conversions cause clouds to optically thicken, producing a major negative feedback. We test this hypothesis by developing a method to decompose cloud radiative feedbacks by cloud-top phase. The method is applied to an ensemble of six state-of-the-art global climate models run with prescribed sea-surface temperature. In these simulations, the global mean of the net cloud scattering and emissivity feedback from cloud-phase conversions ranges from -0.17 to -0.01 W m^{-2} K^{-1}, while the overall net cloud feedback ranges from 0.02 to 0.91 W m^{-2} K^{-1}. The multi-model mean of the cloud scattering and emissivity feedback from cloud-phase conversions is approximately 19% of the magnitude of the multi-model mean of the overall cloud feedback (-0.10 W m^{-2} K^{-1} vs. 0.52 W m^{-2} K^{-1}). These results indicate that cloud-phase conversions cause a robust negative feedback by changing cloud scattering and emissivity, but this mechanism makes a modest contribution to the overall cloud feedback at the global scale.

SIGNIFICANCE STATEMENT

Climate warming changes Earth's cloud properties, which then changes the temperature further. One cloud-climate feedback mechanism involves the conversion of cloud ice particles to liquid droplets with warming. This makes clouds more opaque, causing them to reflect more solar radiation back to space. It is widely accepted that this mechanism dampens climate warming, but its importance relative to other feedback mechanisms has been unclear. This study develops a method to estimate the cloud opacity feedback from ice-to-liquid conversions in climate-model simulations. On average, cloud-opacity changes from phase conversions explain approximately 19% of the overall cloud-climate feedback in an ensemble of six climate models. This finding clarifies the importance of cloud-phase conversions in projections of anthropogenic climate change.

1. Introduction

A central concept in climate science is that the response to an external perturbation can be explained by the sum of individual radiative feedbacks from changes in water vapor, lapse rate, surface albedo, clouds, and other characteristics of the climate system. Among these, the cloud feedback is the largest source of uncertainty in projections of climate sensitivity to CO_2 forcing from comprehensive global climate models (GCMs) (Zelinka et al., 2020; Sherwood et al., 2020; Forster et al., 2021). Reducing this uncertainty is a key goal in climate research.

An extension of this goal is to partition the cloud feedback into contributions from different cloud properties to provide insight into the underlying mechanisms. For instance, Zelinka et al. (2012b) developed a method to partition the cloud feedback in GCM simulations into components from changes in cloud altitude, cloud amount, and cloud visible optical thickness (COT). This method has identified a feedback from rising cloud altitude in the upper troposphere that is simulated by many GCMs and predicted by basic theory (Hartmann and Larson, 2002; Zelinka et al., 2016). Another common feedback across GCMs has been identified from shrinking cloud amount in the subtropical boundary layer due to changes in various meteorological factors (Ceppi et al., 2017). These findings bridge the gap between feedback quantification and physical process understanding.

Feedbacks from changes in COT have been more difficult to explain (Terai et al., 2019). One potential mechanism involves changes in cloud thermodynamic phase. As the atmosphere warms, some cloud condensate that would have been ice in the unperturbed climate is replaced by liquid. Liquid droplets are typically smaller and have a larger surface-area-to-volume ratio than ice particles, so liquid cloud is optically thicker than ice cloud for the same amount of vertically integrated condensate. Pure-liquid clouds also precipitate less efficiently than ice-containing clouds, so ice-to-liquid conversions may reduce precipitation and increase the total cloud condensate (Zhao et al., 2016). The result of these mechanisms is that ice-to-liquid conversions lead to optically thicker and longer lasting clouds that reflect more solar radiation back to space. It has been hypothesized that this may be a powerful negative feedback that can control the sign of the overall cloud feedback simulated by some GCMs, particularly through the change in COT (Li and Le Treut, 1991; Storelvmo et al., 2015; Tan et al., 2016).

Several studies have investigated the cloud-phase feedback with targeted GCM experiments. Mitchell et al. (1989) performed early GCM simulations with one configuration that permitted the cloud-phase feedback to operate and another configuration that did not. They found that activating the configuration that permitted the cloud-phase feedback reduced the equilibrium surface-temperature response to a doubling of atmospheric CO_2 from 5.2 K to 2.7 K. A variety of experiments with variants of the Community Atmosphere Model have also found that configurations with a larger cloud ice water path (IWP) in the preindustrial climate simulate a larger increase in cloud liquid water path (LWP) in response to surface warming and a smaller climate sensitivity to CO_2 forcing, presumably because increasing the preindustrial cloud ice strengthens the cloud-phase feedback (Choi et al., 2014; Ceppi et al., 2016; McCoy et al., 2016; Tan et al., 2016; Frey and Kay, 2018; Bjordal et al., 2020; Zhu et al., 2022; Duffy et al., 2024; Hofer et al., 2024). However, Lohmann and Neubauer (2018) performed perturbed parameter experiments with the ECHAM6-HAM2 GCM and found that preindustrial cloud ice is not systematically related to cloud feedback. Bodas-Salcedo (2018) estimated that phase changes cause less than one third of the midlatitude cloud feedback in the Met Office Unified Model because they mostly occur in optically thick clouds that are not susceptible to increases in albedo. These studies suggest that cloud-phase changes may cause a powerful negative feedback in some GCMs but not others.

Other studies have estimated the cloud-phase feedback with radiative transfer calculations informed by GCM output. McCoy et al. (2015) calculated radiative fluxes above an idealized mixed-phase cloud over the Southern Ocean. In one calculation the cloud was assigned the LWP and IWP averaged over space and time from historical GCM simulations from the Coupled Model Intercomparison Project Phase 5, and in a second calculation the LWP and IWP were changed by equal and opposite amounts. This approach neglects differences in phase changes across cloud regimes, which may bias the feedback estimates (Bodas-Salcedo et al., 2016). Mülmenstädt et al. (2021) avoided this limitation by estimating the cloud-phase feedback with high-frequency output from the ECHAM-HAMMOZ GCM. However, they assumed that ice-to-liquid conversions cause negligible changes in cloud amount and total condensate path outside latitudes of approximately 40° to 70°, thereby neglecting this component of the cloud-phase feedback over 70% of the globe. Furthermore, McCoy et al. (2015) and Mülmenstädt et al. (2021) both estimated the component of the cloud-phase feedback that is caused by changes in phase partitioning over the Southern Ocean,

but their estimates differ by a factor of five. Thus, either the true cloud-phase feedback varies dramatically across GCMs or the estimated feedback is quite sensitive to assumptions in the methodology. This ambiguity makes it difficult to determine the importance of the cloud-phase feedback.

Although these studies provide a qualitative picture of the cloud-phase feedback in GCM simulations, there has not been a rigorous and globally complete assessment of the feedback. Here we address this challenge by developing a method to decompose the cloud feedback by cloud-top phase. The main advantage of the method is that it partitions the COT feedback into components from ice-topped clouds, liquid-topped clouds, mixed-ice-and-liquid-topped clouds, and shifts between these phase categories. The method is applied to six GCMs to quantify the global feedback from changes in cloud scattering and emissivity that is caused by changes in cloud phase. This allows us to test the hypothesis that phase changes cause a powerful negative COT feedback in GCM simulations (Storelvmo et al., 2015; Tan et al., 2016).

2. Data and Methods

a. GCM Simulations

Simulations are performed with the atmosphere and land components of five state-of-the-art GCMs, including the Geophysical Fluid Dynamics Laboratory Atmosphere Model v. 4 (Zhao et al., 2018a; Zhao et al., 2018b), the Energy Exascale Earth System Model v. 2 (Golaz et al., 2022), the Norwegian Earth System Model v. 2.1.1 (Seland et al., 2020), the Model for Interdisciplinary Research on Climate v. 6 (Tatebe et al., 2019), and Community Earth System Model v. 2.1.5 (Danabasoglu et al., 2020). We refer to these models as GFDL, E3SMv2, NorESM2, MIROC6, and CESM2, respectively. Simulations are also performed with a version of MIROC6 in which the standard diagnostic precipitation scheme is replaced by the prognostic precipitation scheme of Michibata et al. (2019). We refer to this model as MIROC6-PP. All of the GCMs except MIROC6-PP have variants that participated in the Coupled Model Intercomparison Project Phase 6 (CMIP6). GFDL, MIROC6, and CESM2 use similar cloud schemes to the CMIP6 versions of the models, and E3SMv2 and NorESM2 use cloud schemes that have been updated from their CMIP6 counterparts in preparation for the Coupled Model Intercomparison Project Phase 7 (Golaz et al., 2022; Olivié, 2024; Debolskiy, 2024). The standard names for the CMIP6

versions of GFDL, E3SMv2, NorESM2, MIROC6, and CESM2 are GFDL-CM4, E3SM-1-0, NorESM2-MM, MIROC6, and CESM2, respectively.

For each GCM, two simulations are performed with prescribed climatological annual cycles of sea-surface temperature and sea-ice fraction. The first simulation represents preindustrial conditions, and the second simulation represents the equilibrium climate state following a sustained doubling of atmospheric CO_2 concentration relative to the preindustrial era. We refer to these simulations as CTL and WARM, respectively. Most of the GCMs had not been run to equilibrium in their fully coupled configurations with these CO_2 concentrations at the time of study, so the sea-surface temperature and sea-ice boundary conditions are obtained from equilibrated simulations of the Geophysical Fluid Dynamics Laboratory CM3 GCM (Donner et al., 2011; Griffies et al., 2011). The surface boundary conditions for CTL are obtained by computing the average annual cycle from the final 100 years of a 4600-year preindustrial control simulation in fully coupled configuration, and the boundary conditions for WARM are obtained by computing the average annual cycle over the same time period from a corresponding simulation with atmospheric CO_2 concentration doubled from the preindustrial value (Fig. 1). The same ocean-surface boundary conditions are applied to all six GCMs. Global-mean surface air temperature is between 4.3 K and 4.7 K warmer in the WARM simulation than the CTL simulation. This quantity varies slightly across models because of differences in surface warming over land. Atmospheric CO_2 concentration is fixed at a preindustrial value of 284 ppmv for both the CTL and WARM simulations. This prevents cloud adjustments to CO_2 forcing and ensures that differences in clouds between the two simulations represent only cloud radiative feedbacks. Simulations are run for at least 10 years to robustly quantify feedbacks, and the first simulation year is discarded for model spin-up (Qin et al., 2022). Model output is linearly interpolated to a common horizontal grid of 1° latitude and 1.25° longitude. The native resolution, simulation length, and primary parameterizations that determine the partitioning of cloud condensate into ice and liquid phases in the GCMs are summarized in Table S1.

All simulations are run with the Moderate Resolution Imaging Spectroradiometer (MODIS) satellite instrument simulator (Bodas-Salcedo et al., 2011; Pincus et al., 2012). This simulator generates synthetic pixel-scale retrievals of cloud-top pressure (CTP), COT, and cloud-top phase that mimic what MODIS would report if it were orbiting above the model atmosphere

(Pincus et al., 2012). Because MODIS is a passive instrument, the retrieved COT represents the total column-integrated cloud optical thickness, and CTP and cloud-top phase represent the top of the highest cloud in the column. The simulator mimics the retrieval limitations of MODIS by reporting data only if sunlight is present and excluding clouds that have a column-integrated COT below 0.3. Synthetic satellite pixels are always either entirely cloud covered or entirely clear sky, so retrieval biases that affect partly cloud-covered pixels in real observations are not present in the MODIS-simulator output. Monthly statistics of the synthetic pixel data are computed over model grid boxes and output for analysis.

We analyze MODIS cloud-property histograms that represent cloud area fraction partitioned by CTP, COT, and cloud-top phase (Fig. 2a-c). The MODIS histograms are similar to the standard histograms from the International Satellite Cloud Climatology Project (ISCCP) except that they are further partitioned by cloud-top phase (Webb et al., 2001; Medeiros et al., 2023; Davis and Medeiros, 2024). Phase is classified based on the condensate between the top of the highest cloud and one optical depth unit below. If the visible extinction in this interval is at least 70% from liquid droplets, then the cloud is classified as liquid. If the visible extinction is at least 70% from ice crystals, then the cloud is classified as ice. If neither or these conditions are satisfied, then the cloud is classified as undetermined phase following the nomenclature of MODIS observational data. Undetermined-phase clouds include true mixed-phase clouds and cases where an ice cloud with COT between 0.3 and 0.7 occurs above a liquid cloud. The thresholds used in this classification are chosen so that the results approximately agree with the real MODIS operational cloud-phase retrieval algorithm (Pincus et al., 2012). The phase-separated CTP-COT joint histograms are developed for this study by modifying the MODIS simulator in the COSPv2.0 software package (CFMIP, 2024). These modifications expand the output variables of the simulator to include new histograms of the synthetic pixel-level retrievals, but they do not change the computations of the pixel-level retrievals themselves.

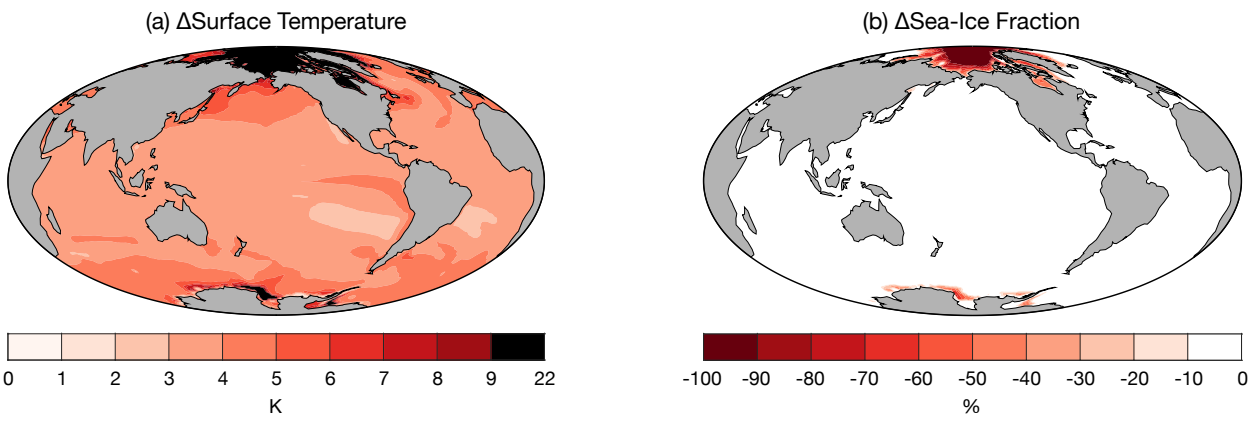

192

193 **Figure 1.** Difference in (a) ocean-surface temperature and (b) sea-ice fraction between the WARM and CTL
194 simulations. The plotted values are annual averages. Surface temperatures represent the average over both open
195 ocean and sea ice. Maps are plotted with a Hammer equal-area projection in all figures.

196

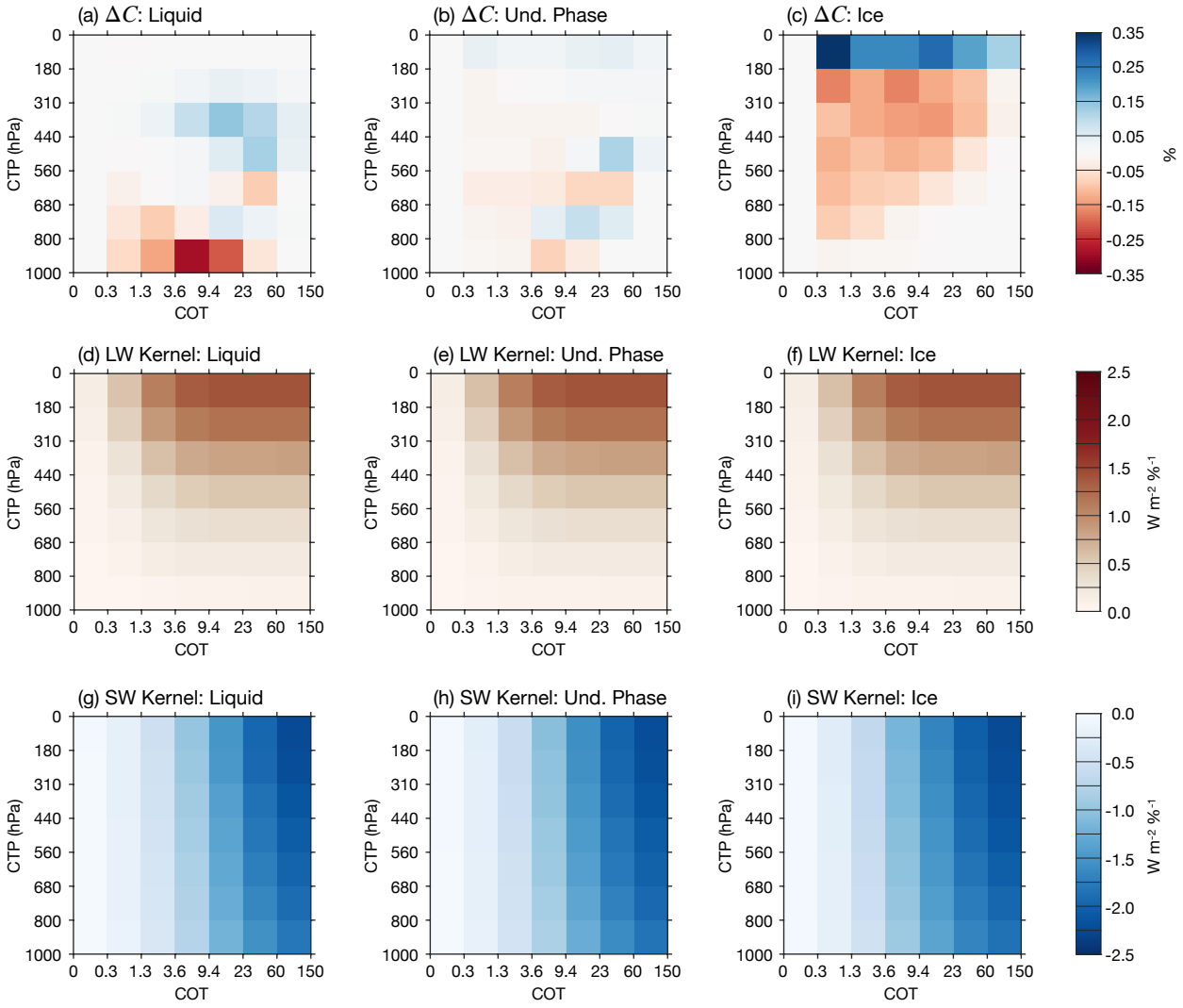

197

198 **Figure 2.** Global- and multi-model-mean of the cloud histograms and radiative kernels. (a-c) Difference in the
199 cloud histograms between the WARM and CTL simulations for liquid-topped clouds, undetermined-phase
200 clouds, and ice-topped clouds, respectively. The units are cloud area fraction (%). (d-f) LW cloud radiative
201 kernels for liquid-topped clouds, undetermined-phase clouds, and ice-topped clouds, respectively. The units are
202 watts per square meter per unit change in cloud area fraction (W m^{-2} $\%^{-1}$). (g-h) Similar to (d-f) but for SW cloud
203 radiative kernels. The histograms and kernels are functions of CTP, COT, cloud-top phase, latitude, longitude,
204 and calendar month, but they have been averaged over the latitude, longitude, and month dimensions for
205 presentation.

206

207 *b. Cloud Radiative Kernels*

Shortwave (SW) and longwave (LW) cloud radiative kernels are computed for the MODIS histograms. The kernels quantify the radiative flux anomaly at the top of the atmosphere that would occur if the cloud fraction in a given histogram bin were to increase by 1% with all non-cloud factors fixed to their average annual cycles. The kernels are similar to those of Zelinka et al. (2012a; hereafter Z12) except that they have an additional dimension of cloud-top phase (Fig. 2d-i). Besides this exception, we compute the kernels by closely following the method of Z12.

The first step of the kernel calculation is to quantify the clear-sky upward SW and LW radiative fluxes at the top of the atmosphere for various combinations of surface albedo, latitude, and calendar month. Calculations are performed with the RRTMG radiative transfer model (Clough et al., 2005) using inputs that include a standard ozone profile; uniform mixing ratios of 330 ppmv, 1.6 ppmv, and 0.28 ppmv for atmospheric CO_2, CH_4, and N_2O, respectively; a uniform surface emissivity of 0.99, and a solar constant of 1361 W m^{-2}. Surface temperature, atmospheric temperature, and specific humidity are prescribed to the average annual cycles from the CTL simulations. These variables are averaged zonally and averaged across the six GCMs before they are input to the radiative transfer model. We then calculate the clear-sky upward LW flux at the top of the atmosphere for each combination of latitude and calendar month. SW fluxes are computed similarly except that surface albedo and insolation are varied to account for surface variations and the diurnal cycle. For a given latitude and calendar month, we chose a day in the middle of the month and calculate the average of the cosine of the solar zenith angle μ for each one-hour interval throughout the day. The clear-sky SW flux is computed for each of the 24 values of μ and then averaged. Calculations are performed with surface albedo of 0, 0.5, and 1. The final result is a matrix of clear-sky upward LW and SW flux at the top of the atmosphere as a function of surface albedo, latitude, and calendar month.

The next step is similar to the clear-sky calculations except that we introduce an overcast and horizontally uniform cloud and systematically vary the CTP, COT, and cloud-top phase. Liquid-topped clouds are assumed to consist entirely of liquid and to have a cloud-droplet effective radius of 10 μm, and the LWP is computed from the COT and cloud-droplet effective radius using Eq. (1) of Slingo (1989). Ice-topped clouds are assumed to consist entirely of ice and to have an ice-crystal effective radius of 30 μm, and IWP is computed from the COT and ice-crystal effective radius using Eq. (3.9a) and Eq. (3.12) of Fu (1996). Undetermined-phase clouds are treated

similarly except that half of the COT is assumed to be associated with ice particles and the other half of the COT is assumed to be associated with liquid droplets. The cloud condensate is placed in a single pressure interval that has a top at the specified CTP. For each latitude, surface albedo, calendar month, and cloud-top phase, we compute the upward SW and LW fluxes at the top of the atmosphere with different combinations of CTP and COT that correspond to the edges of the MODIS histogram bins. Separate calculations are performed for the four edges of each CTP-COT bin, and the results are averaged to get one SW and LW flux value for each bin. The resulting values are subtracted from the clear-sky upward radiative fluxes to determine cloud radiative effects (CRE). The result of these calculations is a matrix of SW CRE and LW CRE above an overcast cloud as a function of latitude, surface albedo, calendar month, CTP, COT, and cloud-top phase.

The final step of the calculation is to convert the overcast-sky CRE to a cloud radiative kernel, K. Let C represent the histogram-partitioned cloud fraction, and let R represent the top-of-atmosphere SW or LW radiative flux. For a given latitude, surface albedo, and calendar month, K represents the radiative flux anomalies caused by changes in C with all non-cloud factors fixed at their average annual cycles:

$$K \equiv \frac{\partial R}{\partial C}.$$

K is computed by dividing the overcast-sky CRE by 100% cloud fraction in order to obtain the radiative flux anomaly averaged over the grid box per unit change in cloud fraction. We apply linear interpolation to transform K from dimensions of latitude and surface albedo to dimensions of latitude and longitude using the average annual cycle of clear-sky surface albedo from the CTL simulations. The interpolation is performed separately for each GCM so that each model has a unique SW kernel that is consistent with its mean-state surface albedo. The final radiative kernels have units of watts per square meter per percentage change in cloud fraction (W m^{-2} $\%^{-1}$) and are functions of latitude, longitude, calendar month, CTP, COT, and cloud-top phase (Fig. 2d-i). The kernels and MODIS histograms reproduce monthly SW, LW, and net CRE anomalies from natural variability with biases of approximately +14%, -8%, and +5%, respectively (Appendix A).

One notable characteristic of the kernel calculation is that COT is prescribed to a set of specific values. Thus, the assumptions about cloud effective radius and phase partitioning in the

kernel calculation affect cloud single-scattering properties, but they do not affect COT. In other words, if the effective radius or phase partitioning is changed when calculating any element of the kernel, then the cloud water path would also be changed in order to keep the COT constant. For this reason, the kernels are similar across the cloud-top phase dimension, and the kernel-based estimates of cloud radiative effects depend weakly on the effective radius and phase partitioning that are assumed in the kernel calculation (Fig. 2d-i; Fig. S1; Table S2; Wall et al., 2022).

c. Estimating Cloud Feedbacks

The MODIS histograms and cloud radiative kernels are used to estimate cloud radiative feedbacks. The total cloud feedback, λ_{cld}, is estimated according to:

$$\lambda_{cld} = \frac{1}{\Delta\langle T_s \rangle} \sum_{p=1}^{7} \sum_{t=1}^{7} \sum_{i=1}^{3} K_{pti} \Delta C_{pti} \quad (1)$$

where Δ represents the difference between the average annual cycles of the WARM and CTL simulations; $\langle T_s \rangle$ is global-mean annual-mean surface air temperature; and p, t, and i correspond to the CTP, COT, and cloud-top phase dimensions of the MODIS histogram, respectively ($i = 1$ for ice-topped clouds, $i = 2$ for liquid-topped clouds, and $i = 3$ for undetermined-phase clouds). Eq. (1) is evaluated for each combination of latitude, longitude, and calendar month, then averaged over the month dimension. An exception is made in polar night because the MODIS simulator does not report data in the absence of sunlight. In this case, the SW feedback is set to zero, and the LW feedback averaged over months with sunlight is assumed to be representative of the LW feedback averaged over the entire year (Z12). Feedback contributions from ice-topped clouds, liquid-topped clouds, and undetermined-phase clouds can be estimated separately by restricting the sum in Eq. (1) to a single cloud-top phase category (i.e. restricting i to a single value).

We also decompose λ_{cld} to isolate the COT feedback from changes in cloud-top phase. The first step of the decomposition is to partition λ_{cld} into a component associated with changes in cloud amount and altitude and a component associated with changes in cloud scattering properties and emissivity. This step is performed separately at each latitude-longitude grid-point for each calendar month and for each CTP bin. Controlling for CTP is particularly important for diagnosing the cloud-phase feedback because it ensures that the feedback estimates represent

phase conversions between clouds at the same pressure level. For a given latitude, longitude, calendar month, and CTP bin p, the total cloud fraction, $C_{tot,p}$, is given by

$$C_{tot,p} = \sum_{t=1}^{7} \sum_{i=1}^{3} C_{pti}.$$

$C_{tot,p}$ can change if either the overall cloud amount changes or if clouds shift vertically from one CTP bin to another. The proportionate change in cloud fraction, $\Delta\hat{C}_{pti}$, is defined by

$$\Delta\hat{C}_{pti} \equiv \Delta C_{tot,p} \frac{\bar{C}_{pti}}{\bar{C}_{tot,p}}$$

where overbars denote values from the average annual cycle of the CTL simulation. This term represents the change in cloud fraction that would occur if $\Delta C_{tot,p}$ were distributed among the COT and cloud-top phase bins such that the proportion of cloud fraction in each bin remains the same as the climatology. In other words, this term represents a change in total cloud-fraction with the normalized distribution of COT and cloud-top phase held fixed. The non-proportionate change in cloud fraction, ΔC^*_{pti}, is the change in cloud fraction that remains after the proportionate change is removed:

$$\Delta C^*_{pti} \equiv \Delta C_{pti} - \Delta\hat{C}_{pti}.$$

This term represents changes in the distribution of COT and cloud-top phase with $C_{tot,p}$ held fixed. Combining these definitions with Eq. (1), λ_{cld} can be expressed as

$$\lambda_{cld} = \underbrace{\left[\frac{1}{\Delta\langle T_s\rangle} \sum_{p=1}^{7} \sum_{t=1}^{7} \sum_{i=1}^{3} K_{pti} \Delta\hat{C}_{pti}\right]}_{\lambda_{\Delta amt+\Delta alt}} + \underbrace{\left[\frac{1}{\Delta\langle T_s\rangle} \sum_{p=1}^{7} \sum_{t=1}^{7} \sum_{i=1}^{3} K_{pti} \Delta C^*_{pti}\right]}_{\lambda_{\Delta se}} \quad (2)$$

where $\lambda_{\Delta amt+\Delta alt}$ is the feedback from changes in cloud amount and altitude and $\lambda_{\Delta se}$ is the feedback from changes in cloud scattering properties and emissivity. We refer to $\lambda_{\Delta se}$ as the "cloud scattering and emissivity feedback" because it represents changes in COT and cloud single-scattering properties, although it is dominated by changes in COT.

We next partition $\lambda_{\Delta se}$ into a component caused by changes in cloud-top phase and a component caused by changes in COT within each cloud-top-phase category. Let $\overline{\boldsymbol{C}}_{pi}$ be the climatological cloud fraction summed over the COT dimension for a given CTP bin p and cloud-top phase category i:

$$\overline{\boldsymbol{C}}_{pi} = \sum_{t=1}^{7} \bar{C}_{pti}.$$

Similarly, let $\Delta \boldsymbol{C}^{*}_{pi}$ be the non-proportionate change in cloud fraction summed over the COT dimension:

$$\Delta \boldsymbol{C}^{*}_{pi} = \sum_{t=1}^{7} \Delta C^{*}_{pti}.$$

We define ΔC^{**}_{pti} by

$$\Delta C^{**}_{pti} \equiv \Delta C^{*}_{pti} - \Delta \boldsymbol{C}^{*}_{pi} \frac{\bar{C}_{pti}}{\overline{\boldsymbol{C}}_{pi}}.$$

By construction, the sum of $\Delta \boldsymbol{C}^{*}_{pi}$ over the cloud-top-phase categories is equal to zero for each CTP bin. Thus, the term $\Delta \boldsymbol{C}^{*}_{pi} \frac{\bar{C}_{pti}}{\overline{\boldsymbol{C}}_{pi}}$ represents shifts in cloud fraction between the phase categories holding fixed the overall cloud-fraction summed over all phase categories and the normalized COT distribution of each phase category. ΔC^{**}_{pti} is the change in cloud fraction that remains after the shifts in cloud fraction between phase categories are removed from the non-proportionate change in cloud fraction (ΔC^{*}_{pti}). ΔC^{**}_{pt1} represents changes in the COT distribution of ice-topped clouds with the overall ice-topped cloud-fraction held fixed, ΔC^{**}_{pt2} represents changes in the COT distribution of liquid-topped clouds with the overall liquid-topped cloud-fraction held fixed, and ΔC^{**}_{pt3} represents changes in the COT distribution of undetermined-phase clouds with the overall undetermined-phase cloud-fraction held fixed. By substituting this relationship for ΔC^{*}_{pti} in Eq. (2), $\lambda_{\Delta se}$ can be expressed as

$$\lambda_{\Delta se} = \underbrace{\left[\frac{1}{\Delta\langle T_s\rangle}\sum_{p=1}^{7}\sum_{t=1}^{7}\sum_{i=1}^{3} K_{pti}\,\Delta \boldsymbol{C}^{*}_{pi}\,\frac{\bar{C}_{pti}}{\overline{\boldsymbol{C}}_{pi}}\right]}_{\lambda_{tot,phase}} + \underbrace{\left[\frac{1}{\Delta\langle T_s\rangle}\sum_{p=1}^{7}\sum_{t=1}^{7} K_{pt1}\Delta C^{**}_{pt1}\right]}_{\lambda_{\Delta COT,ice}}$$
$$+ \underbrace{\left[\frac{1}{\Delta\langle T_s\rangle}\sum_{p=1}^{7}\sum_{t=1}^{7} K_{pt2}\Delta C^{**}_{pt2}\right]}_{\lambda_{\Delta COT,liq}} + \underbrace{\left[\frac{1}{\Delta\langle T_s\rangle}\sum_{p=1}^{7}\sum_{t=1}^{7} K_{pt3}\Delta C^{**}_{pt3}\right]}_{\lambda_{\Delta COT,und}}. \quad (3)$$

$\lambda_{tot,phase}$ represents the feedback from changes in cloud scattering and emissivity that is caused by changes in cloud-top phase. $\lambda_{\Delta COT,ice}$, $\lambda_{\Delta COT,liq}$, and $\lambda_{\Delta COT,und}$ represent feedbacks from changes in the COT of ice-topped clouds, liquid-topped clouds, and undetermined-phase clouds, respectively.

In the derivation of $\lambda_{tot,phase}$, $\lambda_{\Delta COT,ice}$, $\lambda_{\Delta COT,liq}$, and $\lambda_{\Delta COT,und}$, we have assumed that all cloud elements have an equal probability of undergoing a cloud-top-phase conversion within each CTP-phase-latitude-longitude-month combination. In other words, we ignore any possible relationship between the optical thickness of ice-topped clouds and their susceptibility to a cloud-top-phase conversion. Liquid-topped clouds and undetermined-phase clouds are treated similarly. This assumption affects the partitioning of $\lambda_{\Delta se}$ into components, but it does not affect the overall value of $\lambda_{\Delta se}$.

The feedback component $\lambda_{tot,phase}$ occurs because cloud-phase conversions change COT and the single-scattering properties of cloud particles, including the single-scattering albedo ω and the asymmetry factor g (Wall et al., 2022). ω represents the probability that a photon is scattered given that a single extinction event occurs, and g embodies the typical scattering angles of cloud particles in single scattering events. We disentangle these factors by partitioning $\lambda_{tot,phase}$ into a component associated with changes in COT and a component associated with changes in g and ω. For a given CTP bin p, let $\widetilde{K}_{tp}$ be the cloud radiative kernel averaged across the cloud-top phase categories weighted by their average frequency of occurrence:

$$\widetilde{K}_{pt} \equiv \frac{\sum_{i=1}^{3} \overline{\boldsymbol{C}}_{pi} K_{pti}}{\sum_{i=1}^{3} \overline{\boldsymbol{C}}_{pi}}.$$

The kernel can then be decomposed into two terms:

$$K_{pti} = \widetilde{K}_{pt} + \left(K_{pti} - \widetilde{K}_{pt}\right).$$

The term $\widetilde{K}_{pt}$ quantifies the radiative impact of changes in the histogram-partitioned cloud-fraction with g and ω fixed to the frequency-weighted average across the cloud-top-phase categories. The term $(K_{pti} - \widetilde{K}_{pt})$ quantifies the variation in the cloud radiative kernels across the cloud-top-phase categories due to differences in g and ω with COT held fixed. Thus, $\lambda_{tot,phase}$ can be expressed as

$$\lambda_{tot,phase} = \underbrace{\left[\frac{1}{\Delta\langle T_s\rangle}\sum_{p=1}^{7}\sum_{t=1}^{7}\sum_{i=1}^{3}\widetilde{K}_{pt}\Delta\boldsymbol{C}^{*}_{pi}\frac{\bar{C}_{pti}}{\overline{\boldsymbol{C}}_{pi}}\right]}_{\lambda_{\Delta COT,phase}} + \underbrace{\left[\frac{1}{\Delta\langle T_s\rangle}\sum_{p=1}^{7}\sum_{t=1}^{7}\sum_{i=1}^{3}(K_{pti} - \widetilde{K}_{pt})\Delta\boldsymbol{C}^{*}_{pi}\frac{\bar{C}_{pti}}{\overline{\boldsymbol{C}}_{pi}}\right]}_{\lambda_{\Delta g+\Delta\omega,phase}} \quad (4)$$

where $\lambda_{\Delta COT,phase}$ and $\lambda_{\Delta g+\Delta\omega,phase}$ are the components of the feedback from cloud-top phase conversions that are caused by changes in COT and cloud single-scattering properties, respectively.

Combining Eq. (1-4) yields the final cloud-feedback decomposition:

$$\lambda_{cld} = \lambda_{\Delta amt+\Delta alt} + \lambda_{\Delta COT,phase} + \lambda_{\Delta g+\Delta\omega,phase} + \lambda_{\Delta COT,ice} + \lambda_{\Delta COT,liq} + \lambda_{\Delta COT,und}. \quad (5)$$

λ_{cld} is partitioned entirely among the terms on the right side of Eq. (5) without a residual. Furthermore, the decomposition is performed separately for each combination of CTP, latitude, longitude, and calendar month, so it does not assume that any of the terms are restricted to a particular temperature range.

This method quantifies the cloud scattering and emissivity feedback like other methods that are commonly applied to GCM output (Taylor et al., 2007; Zelinka et al., 2012b; Zelinka et

al., 2013). The main advantage of the new method is that it also decomposes the cloud scattering and emissivity feedback as a function of cloud-top phase and shifts between cloud-top phase categories. Similar methods have been developed to decompose cloud radiative effects by cloud-top phase in satellite observations (Tan et al., 2019; Zhou et al., 2022; Wall et al., 2022). Our method applies this concept to cloud radiative feedbacks in GCM simulations.

d. Comparison with other Feedback Analyses and the CMIP6 Ensemble

Our cloud-feedback analysis differs from previous analyses in several ways. The main differences include the input data, the mathematical framework of the feedback decomposition, and the GCMs that are analyzed. We examine these differences to frame the analysis in the context of the existing literature.

First, our method is based on the established method of Z12, but we estimate λ_{cld} with different input data. Z12 use ISCCP-simulator output, while we use MODIS-simulator output. ISCCP generally reports CTP at the infrared emission level located about one optical depth below the cloud top, while MODIS reports CTP at a higher altitude that is closer to the true cloud top (Pincus et al., 2012). The offset between the CTP reported by MODIS and the infrared emission level may cause a bias in the LW cloud feedback estimated with MODIS data. The ISCCP simulator also reports clouds of all optical thicknesses, while the MODIS simulator reports clouds with COT $\geq$ 0.3 (Pincus et al., 2012). The fact that the MODIS simulator excludes clouds with COT < 0.3 may bias the estimates of cloud feedbacks. However, the bias in global net cloud feedback is about 3% or less in our simulations, and it is negligible in most CMIP6 models (Table S3; Chao et al., 2024). Finally, the cloud radiative kernels of Z12 are computed with temperature and humidity profiles from a different set of GCMs. These differences could affect the estimates of λ_{cld} in some situations.

We validate our method based on its ability to reproduce λ_{cld} estimated with the Z12 method. Five of the six GCMs reported ISCCP-simulator output, so we compare feedbacks from these five models (all but GFDL). The spatial patterns of feedbacks computed by the two methods have strong point-by-point correlations (Fig. 3). The squared coefficient of determination (R^2) is at least 0.97 for the SW cloud feedback and at least 0.84 for the LW cloud feedback in all of the GCMs. The global-mean cloud feedback across the five GCMs agrees to within 0.12 W m^{-2} K^{-1} for SW radiation and 0.15 W m^{-2} K^{-1} for LW radiation. Feedback estimates from our method also

agree closely with feedback estimates from the approximate partial radiative perturbation method (Taylor et al., 2007) (Fig. S2). Thus, our method accurately reproduces the overall cloud feedback estimated by other established methods.

A second distinction of our method is that it decomposes the cloud feedback separately for each CTP bin. This differs from conventional cloud-feedback decompositions, which have much coarser CTP resolution or do not resolve feedbacks by CTP at all (Taylor et al., 2007; Zelinka et al., 2012b; Zelinka et al., 2013; Zelinka et al., 2016). The choice of decomposing feedbacks over broad or narrow CTP intervals does not affect the quantification of the overall cloud feedback, but it can affect the partitioning among feedback components in cases where clouds at different pressure levels respond differently to surface warming (Zelinka et al., 2016). Indeed, the overall cloud feedback computed with our method agrees very well with the overall cloud feedback computed with the method of Zelinka et al. (2016), but the two methods partition the feedback slightly differently into amount, altitude, and COT components (Appendix B).

Despite this difference, we chose to partition feedbacks separately for each CTP bin because this ensures that the estimated cloud-phase feedback represents phase conversions between clouds at the same pressure level. An alternative choice could be to combine all clouds across a broad CTP range that spans the upper and lower troposphere and then apply the feedback decomposition of Eq. (1-5) on the aggregated data. However, if one were to follow this procedure in a case where ice-topped clouds change in the upper troposphere and liquid-topped clouds change in the lower troposphere, then these cloud changes could contribute to the estimated COT feedback from cloud-phase conversions ($\lambda_{tot,phase}$), even though they occur at different pressure levels and do not represent one phase replacing the other. We chose to decompose feedbacks separately for each CTP bin to avoid this limitation and quantify the cloud-phase feedback as accurately as possible. Different choices could be justified for quantifying other feedback components (Appendix C).

Finally, we analyze output from six GCMs, so the feedbacks may differ from those in more diverse model ensembles. However, our ensemble includes model variants from three of the 12 model families in CMIP6 that have been identified based on source-code development (Kuma et al., 2023). GFDL belongs to one family; MIROC6 and MIROC6-PP belong to a second family; and CESM2, NorESM2, and E3SMv2 belong to a third family. Furthermore, the diversity of our ensemble can be examined based on the range of global net cloud feedback and the estimated

equilibrium climate sensitivity (ECS), which represents the long-term global surface-air-temperature change following a sustained doubling of atmospheric CO_2 concentration relative to the preindustrial era. These quantities are obtained from published estimates from fully coupled versions of the models or their closest predecessor in CMIP6 (Zelinka et al., 2020; Golaz et al., 2022; Qin et al., 2024). Estimates from fully coupled simulations were not available for MIROC6-PP, so estimates from simulations with prescribed sea surface temperature are used instead (Hirota et al., 2022). The ECS for the model variants related to our ensemble ranges from 2.49 to 5.15 K, and the global net cloud feedback ranges from 0.12 to 0.96 W m^{-2} K^{-1}. These ranges span most of the full ensemble of 53 fully coupled CMIP6 models estimated by Zelinka et al. (2020) (Fig. 4). The six-member ensemble is thus a representative subset of CMIP6-era atmospheric models. The ensemble may not be representative of the Coupled Model Intercomparison Project Phase 5, however, because those models generally simulate a different phase partitioning in mixed-phase clouds (Zelinka et al., 2020).

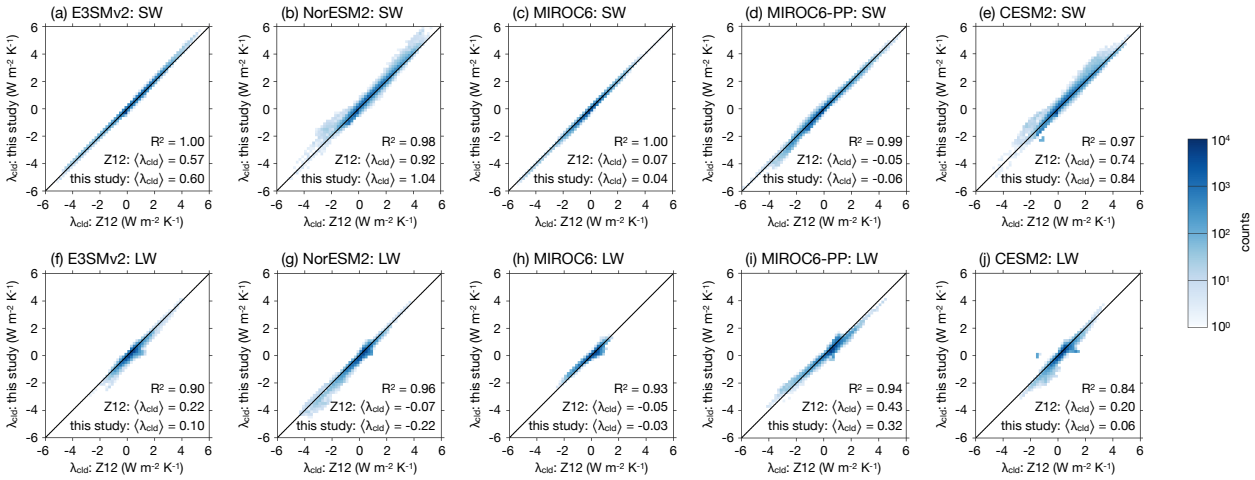

Figure 3. Point-by-point comparison of the overall cloud feedback (λ_{cld}) computed with the method of this study and the method of Zelinka et al. (2012a) (Z12). (a-e) Joint histogram of SW cloud feedback from the two methods in E3SMv2, NorESM2, MIROC6, MIROC6-PP, and CESM2, respectively. Blue shading shows the number of latitude-longitude grid-points in the histogram bins on a logarithmic color scale, and the diagonal shows the one-to-one line. The bottom right corner of each panel lists the global-mean feedback ($\langle\lambda_{cld}\rangle$) in units of W m^{-2} K^{-1} and the squared coefficient of determination for the ordinary least-squares linear-regression fit (R^2). (f-j) Similar to (a-e) but for the LW cloud feedback. The GFDL model is not shown because the necessary output to compute feedbacks with the Z12 method is not available.

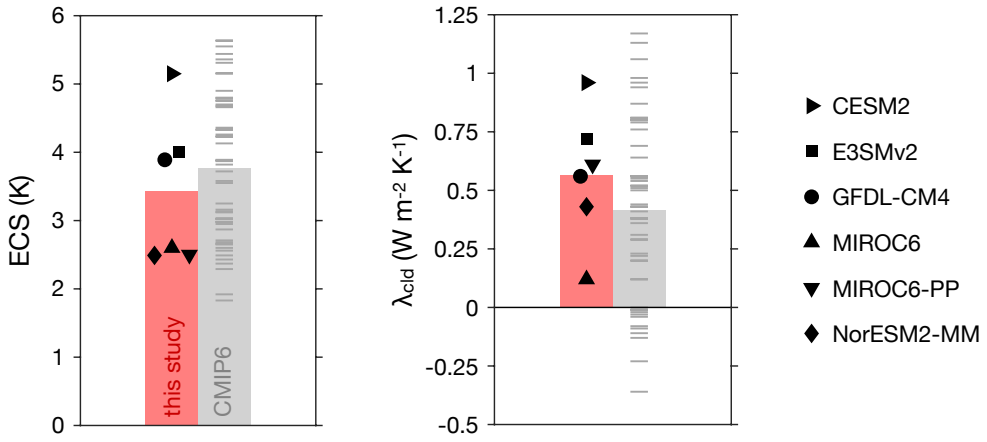

456

457 **Figure 4.** Published estimates of equilibrium climate sensitivity (ECS) and global net cloud feedback (λ_{cld}) for
458 variants of the GCMs analyzed in this study and CMIP6. Black markers show variants of the GCMs analyzed in
459 this study, thin horizontal lines show CMIP6 models, and bars show the multi-model mean. The models labeled
460 CESM2, GFDL-CM4, MIROC6, and NorESM2-MM are CMIP6 versions of the GCMs analyzed in this study.
461 The models E3SMv2 and MIROC6-PP are not in the CMIP6 ensemble. All of the estimates come from fully
462 coupled model configurations except for MIROC6-PP, which was run with prescribed sea surface temperature.
463 Estimates for E3SMv2 are from Golaz et al. (2022) and Qin et al. (2024), estimates for MIROC6-PP are from
464 Hirota et al. (2022), and estimates for the remaining models are from Zelinka et al. (2020).
465

466 **3. Results**

467 *a. Decomposing Feedbacks by Cloud-Top Phase*

468 We next examine the cloud-feedback decomposition across the GCM ensemble. Global-
469 mean feedbacks are reported as $[\lambda] \pm \sigma_\lambda$, where $[\lambda]$ is the multi-model mean of the global feedback
470 and σ_λ is the standard deviation of the global feedback across the model ensemble. The total global-
471 mean SW cloud feedback is 0.42 ± 0.47 W m^{-2} K^{-1}. This feedback arises from a combination of a
472 negative SW feedback in the polar regions, a positive SW feedback over the midlatitude oceans,
473 and spatially varying positive and negative feedbacks in the tropics (Fig. 5a). The overall SW
474 feedback includes a component from changes in cloud amount and altitude of 0.38 ± 0.42 W m^{-2}
475 K^{-1} and a component from changes in cloud scattering properties and emissivity of 0.03 ± 0.13 W
476 m^{-2} K^{-1}. The SW cloud amount and altitude component explains much of the spatial pattern and
477 global mean of the SW cloud feedback, but the cloud scattering and emissivity component is

substantial in the polar regions and deep tropics (Fig. 5b-c). The LW cloud-feedback components are generally smaller and vary less across models than their SW counterparts (Fig. 5d-f). Thus, the cloud amount and altitude component of the feedback dominates the net cloud feedback at the global scale. This component is also dominant in the feedback decomposition of Zelinka et al. (2016) (Fig. B1).

The SW cloud amount and altitude feedback over the midlatitude oceans makes a particularly large contribution to the global cloud feedback in the multi-model mean (Fig. 5b). This is consistent with the simulations of the GFDL-CM3 GCM of Paynter et al. (2018), from which the surface boundary conditions of our simulations are obtained. They noted that CO_2 forcing caused long-term changes of the atmosphere and surface that weakened the boundary layer inversion strength over midlatitude oceans. This, in turn, reduced the low-level cloud amount and caused a major positive SW cloud feedback. Zhao (2022) also found that the atmospheric component of GFDL-CM3 simulates a reduction in low-level cloud amount over midlatitude oceans when forced by a variety of prescribed surface warming patterns. The fact that our simulations exhibit a positive SW cloud feedback over midlatitude oceans without a compensating LW feedback suggests that reduced low-level cloud amount in the midlatitudes causes a major global feedback in our simulations as well.

Although the cloud scattering and emissivity feedback is a small component of the overall global cloud feedback, previous work suggests that it may involve multiple compensating mechanisms that are individually substantial (Terai et al., 2019). We examine this possibility by decomposing the cloud scattering and emissivity feedback by cloud-top phase. Changes in cloud scattering and emissivity cause a negative SW feedback over polar regions and land areas of the middle and high latitudes, a positive SW feedback over midlatitude oceans, and dipole patterns of feedbacks near the equator (Fig. 6a). This can mostly be explained by four terms in the feedback decomposition. First, changes in cloud-top phase cause clouds to optically thicken, producing a global SW feedback of -0.15 ± 0.08 W m^{-2} K^{-1}. This negative feedback is present in nearly all areas of the globe, and it is strongest in the extratropical storm tracks and tropical warm pools (Fig. 6b). Second, changes in cloud-top phase modify the cloud single-scattering properties (g and ω), producing a global SW feedback of 0.03 ± 0.01 W m^{-2} K^{-1} (Fig. 6c). This component represents the fact that ice particles typically backscatter more SW radiation than liquid droplets in single-

particle scattering events, so converting ice to liquid enhances forward scattering. This reduces the cloud albedo if the COT is fixed, causing a positive SW feedback (Wall et al., 2022). Third, changes in the optical thickness of ice-topped clouds contribute a positive global SW feedback of 0.17 ± 0.14 W m^{-2} K^{-1}. This feedback is positive over most of the globe, indicating that ice-topped clouds become optically thinner (Fig. 6d). One exception is the dipole patterns along the equator, which may result from spatial shifts or contraction of the Intertropical Convergence Zone. Fourth, changes in the optical thickness of liquid-topped clouds contribute a global SW feedback of -0.02 ± 0.04 W m^{-2} K^{-1}. This term dominates the SW cloud scattering and emissivity feedback in polar regions but is less important across the non-polar regions in the multi-model mean (Fig. 6e). SW feedbacks from changes in COT of undetermined-phase clouds are relatively small (Fig. 6f). The total LW cloud scattering and emissivity feedback is smaller than its SW counterpart and is dominated by changes in the optical thickness of ice-topped clouds (Fig. 7).

The spatial patterns of the feedback components suggest that different feedback mechanisms may be active at different locations and pressure levels in the atmosphere. To explore this possibility, we compute zonal-mean feedbacks averaged over 10° latitude bands and plot the results as a function of latitude and CTP. Indeed, distinct cloud feedbacks occur in the mixed-phase temperature range of -40 to 0 °C (Fig. 8a). These feedbacks are mostly caused by cloud optical thickening from cloud-top phase conversions (Fig. 8b). Changes in cloud single-scattering properties (g and ω) from phase conversions contribute a relatively small positive feedback as well (Fig. 8c). Finally, liquid-topped clouds with CTP between the surface and 560 hPa become optically thicker in the polar regions, causing a robust negative SW feedback (Fig. 8e). This could be a consequence of cloud-phase conversions in the interior of liquid-topped mixed-phase clouds, enhanced condensation in the updrafts of supercooled liquid clouds due to changes in the moist adiabatic lapse rate, or enhanced moisture flux convergence in extratropical cyclones (Betts and Harshvardhan, 1987; Terai et al., 2019; McCoy et al., 2020; Frazer and Ming, 2022; McCoy et al., 2023). These feedback components combine to produce a negative SW cloud scattering and emissivity feedback throughout most of the mixed-phase temperature range. The SW feedbacks are partially compensated by their LW counterparts (Fig. 9).

The feedback decomposition stratified by latitude and CTP also reveals a substantial positive SW feedback and a smaller negative LW feedback from optical thinning of ice-topped

clouds in the tropical upper troposphere (Fig. 8d, 9d). One possible explanation is that surface warming weakens the tropical overturning circulation, reducing the amount of optically thick ice clouds detrained from deep convection (Jeevanjee, 2022). At the same time, the weaker overturning circulation could cause smaller changes in the amount of optically thin ice clouds that are not directly formed by convection. The combination of these changes would cause optically thick ice clouds to disproportionately shrink in amount, thereby causing the overall ice-cloud population to become optically thinner (Sokol et al., 2024). This possible explanation is examined in Appendix C. Indeed, five out of the six GCMs simulate a reduced ice-cloud fraction in the tropical upper troposphere in response to surface warming, and the reduction is disproportionately large for clouds that are not optically thin (COT $\geq$ 3.6) (Fig. C1a). The proportion of ice-topped clouds that are optically thin (0.3 $\leq$ COT < 3.6) also increases in response to surface warming in all six GCMs (Fig. C1b). The fact that these changes are consistent across models and consistent with an expected weakening of the tropical overturning circulation suggests that an optical thinning of tropical ice clouds may be a robust feedback mechanism. However, sensitivity tests indicate that our method probably exaggerates the magnitude of the ice-cloud COT feedback due to confounding factors from vertical shifts in ice clouds (Fig. C2). The ice-cloud COT feedback estimated here should thus be interpreted with caution.

The feedback components can be vertically integrated and globally averaged to determine their relative importance at the global scale. Two groups of feedback components emerge in which all models agree on the sign (Fig. 10). The first group involves changes in cloud-top phase. This group includes a negative SW feedback from changes in COT (-0.15 ± 0.08 W m^{-2} K^{-1}), a positive LW feedback from changes in COT (0.04 ± 0.02 W m^{-2} K^{-1}), and a positive SW feedback from changes in cloud single-scattering properties (0.03 ± 0.01 W m^{-2} K^{-1}). Previous studies have focused on the SW COT component of this feedback, while the LW COT and SW single-scattering components have been given less attention. Although the SW COT feedback is the largest of these terms, the other two terms collectively offset about half of the SW COT feedback, so they make a non-negligible contribution to the cloud-phase feedback. The second group of feedback components involves optical thinning of ice-topped clouds. This causes a positive SW feedback of 0.17 ± 0.14 W m^{-2} K^{-1} and a negative LW feedback of -0.06 ± 0.05 W m^{-2} K^{-1}. The feedback

components of these two groups offset one another, causing the net cloud scattering and emissivity feedback to take on a relatively small value of 0.02 ± 0.09 W m^{-2} K^{-1} (Fig. 10).

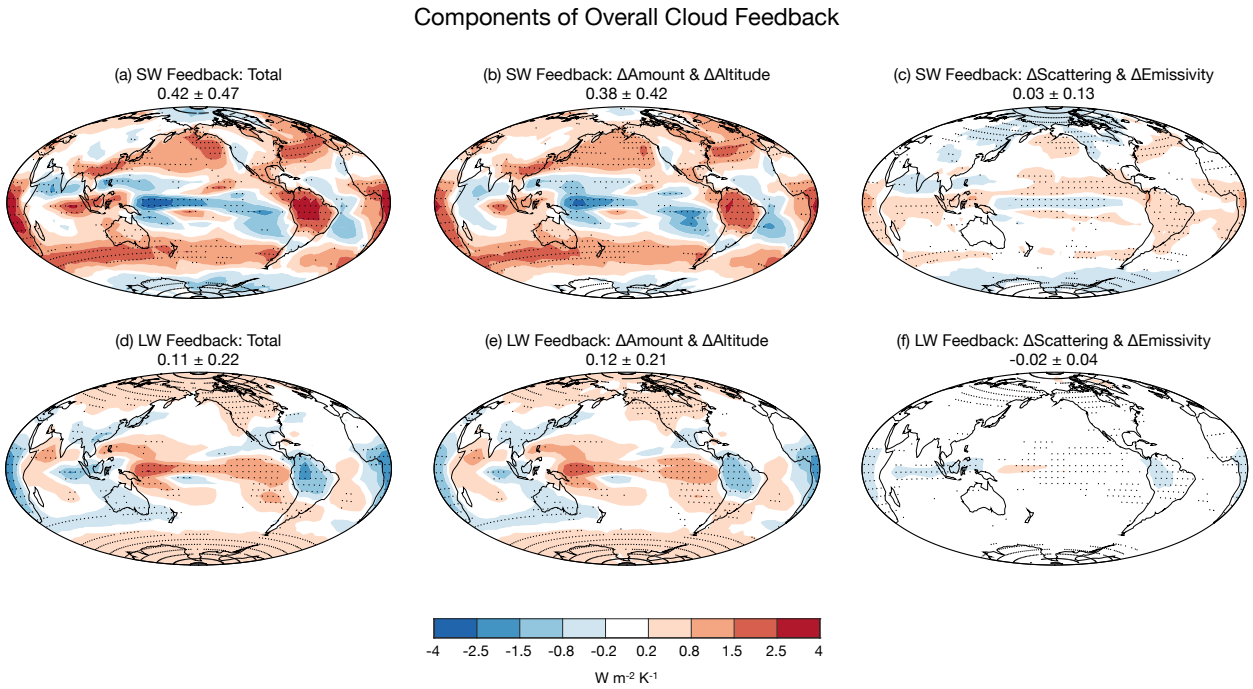

Figure 5. Components of the overall cloud feedback, including (a) the total SW cloud feedback (λ_{cld}), (b) the SW feedback from changes in cloud amount and cloud altitude ($\lambda_{\Delta amt+\Delta alt}$), and (c) the SW feedback from changes in cloud scattering properties and emissivity ($\lambda_{\Delta se}$). Contours show the multi-model mean feedback, and dots show locations where all models agree on the feedback sign. The global-mean feedback is printed above each map in units of W m^{-2} K^{-1} . The printed value is the multi-model mean plus or minus the ensemble standard deviation. (d-f) Similar to (a-c) but for LW feedbacks. Contour values are spaced nonuniformly to show components that have relatively small magnitudes. A similar figure with uniform contour spacing is shown in Fig. S3.

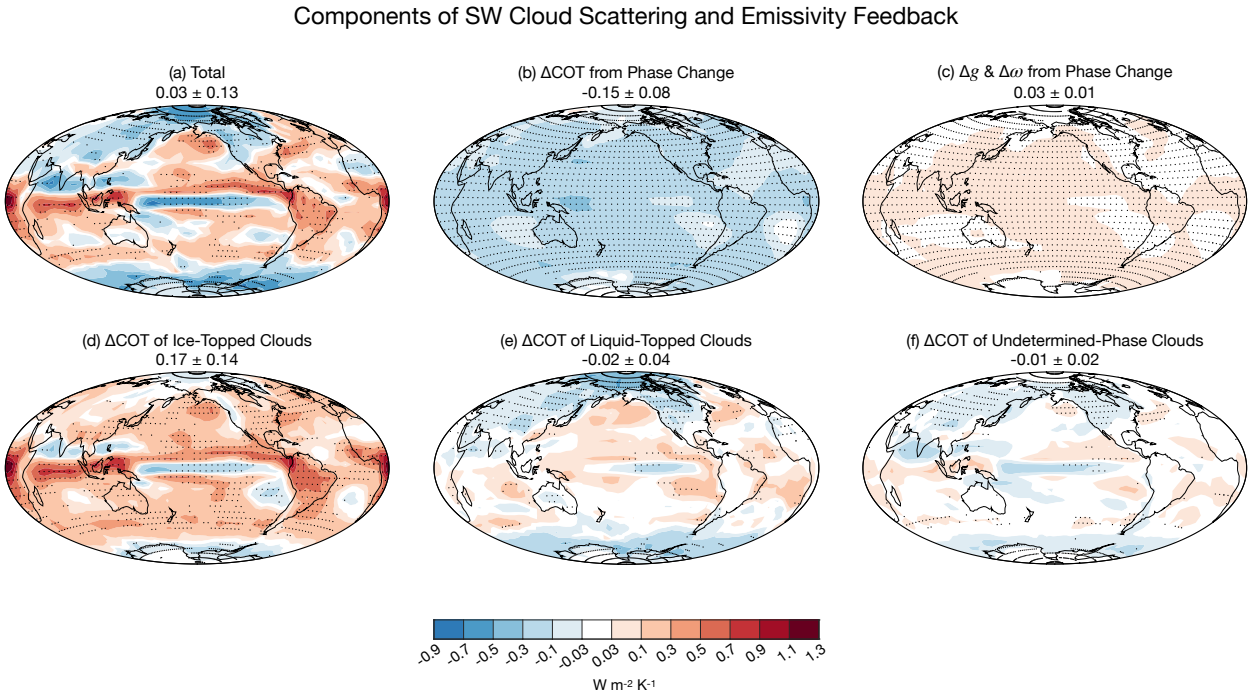

580

581 **Figure 6.** Components of the SW cloud scattering and emissivity feedback, including (a) the total cloud
582 scattering and emissivity feedback ($\lambda_{\Delta se}$), (b) the COT feedback from cloud-top phase changes ($\lambda_{\Delta COT,phase}$),
583 (c) the cloud single-scattering properties feedback from cloud-top phase changes ($\lambda_{\Delta g+\Delta\omega,phase}$), (d) the COT
584 feedback of ice-topped clouds ($\lambda_{\Delta COT,ice}$), (e) the COT feedback of liquid-topped clouds ($\lambda_{\Delta COT,liq}$), and (f) the
585 COT feedback of undetermined-phase clouds ($\lambda_{\Delta COT,und}$). The global-mean feedback is printed above each map
586 in units of W m^{-2} K^{-1} . The printed value is the multi-model mean plus or minus the ensemble standard deviation.
587 Contour values are spaced nonuniformly to show components that have relatively small magnitudes. A similar
588 figure with uniform contour spacing is shown in Fig. S4.

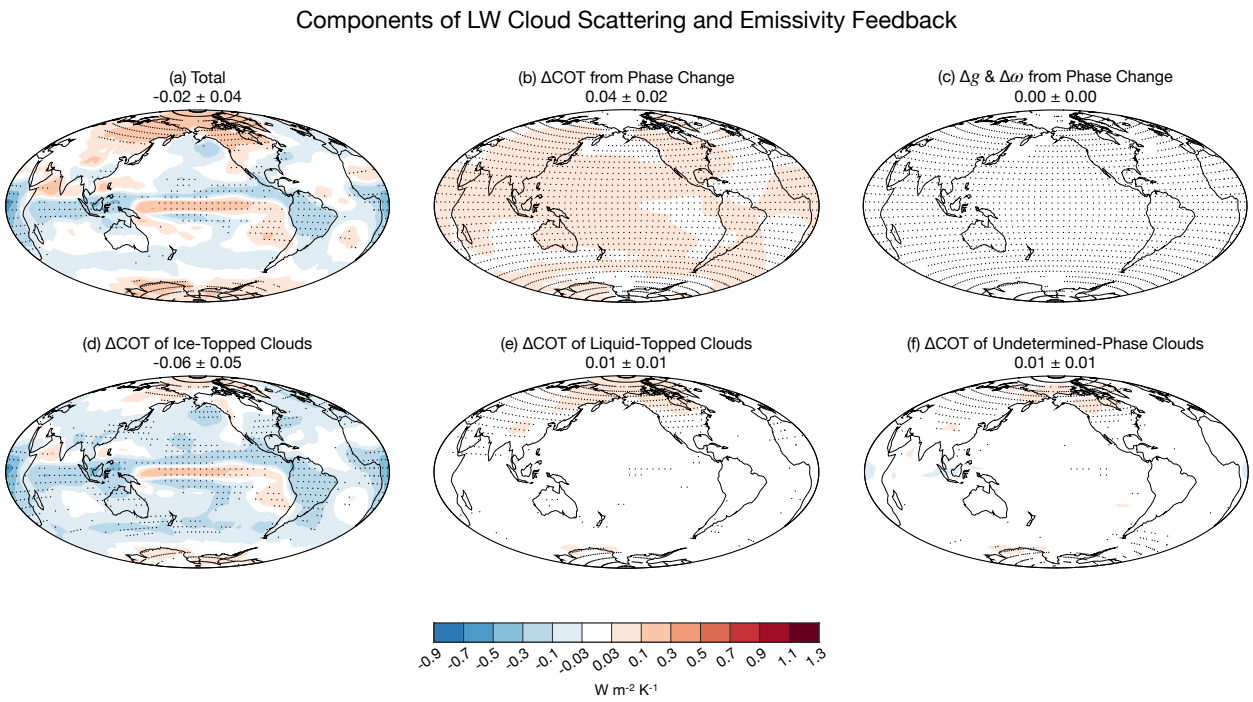

589

590 **Figure 7.** Similar to Fig. 6, but for the LW cloud scattering and emissivity feedback. Contour values are spaced
591 nonuniformly to show components that have relatively small magnitudes. A similar figure with uniform contour
592 spacing is shown in Fig. S5.

593

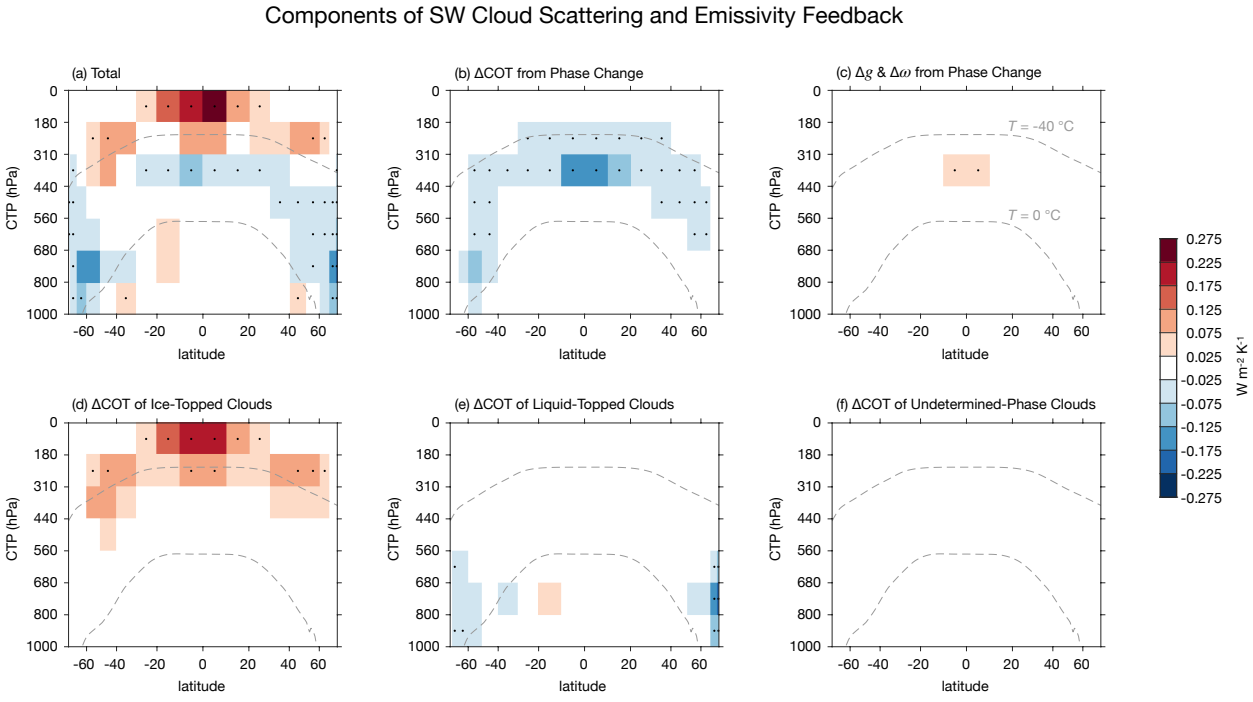

594

595 **Figure 8.** Components of the SW cloud scattering and emissivity feedback averaged zonally and plotted as a
596 function of latitude and CTP. The components include (a) the total cloud scattering and emissivity feedback
597 ($\lambda_{\Delta se}$), (b) the COT feedback from cloud-top phase changes ($\lambda_{\Delta COT,phase}$), (c) the cloud single-scattering
598 properties feedback from cloud-top phase changes ($\lambda_{\Delta g+\Delta\omega,phase}$), (d) the COT feedback of ice-topped clouds
599 ($\lambda_{\Delta COT,ice}$), (e) the COT feedback of liquid-topped clouds ($\lambda_{\Delta COT,liq}$), and (f) the COT feedback of undetermined-
600 phase clouds ($\lambda_{\Delta COT,und}$). Colors show the multi-model mean feedback, and dots show locations where all
601 models agree on the feedback sign and the multi-model mean has a magnitude larger than 0.025 W m^{-2} K^{-1} (non-
602 white colors on the color scale). The lower dashed gray line shows the 0 °C isotherm from the temperature profile
603 of the CTL simulation averaged over longitude, the annual cycle, and the six GCMs. The upper dashed gray line
604 is similar but shows the -40 °C isotherm from the WARM simulation. Feedbacks from cloud-top phase
605 conversions are expected to be strongest between the two isotherms because points located outside of this region
606 are either warmer than 0 °C or colder than -40 °C in both simulations. Latitude axes are presented in equal-area
607 increments.

608

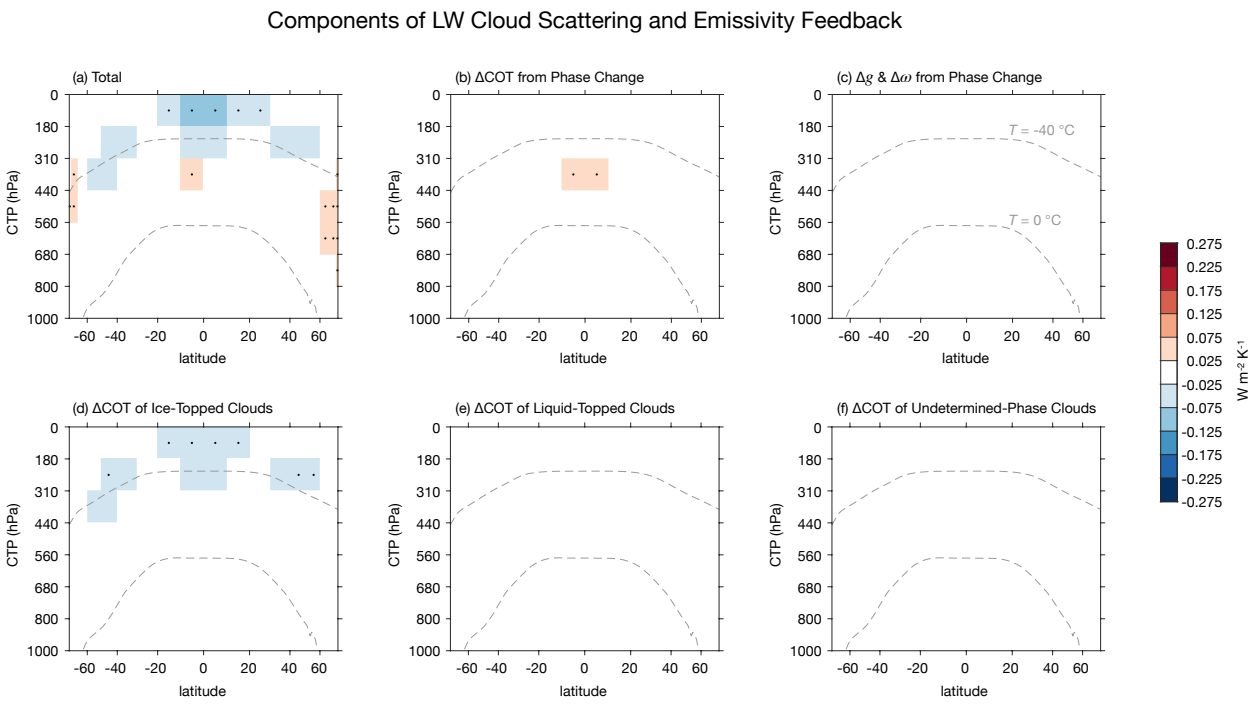

609

610 **Figure 9.** Similar to Fig. 8, but for the LW cloud scattering and emissivity feedback.

611

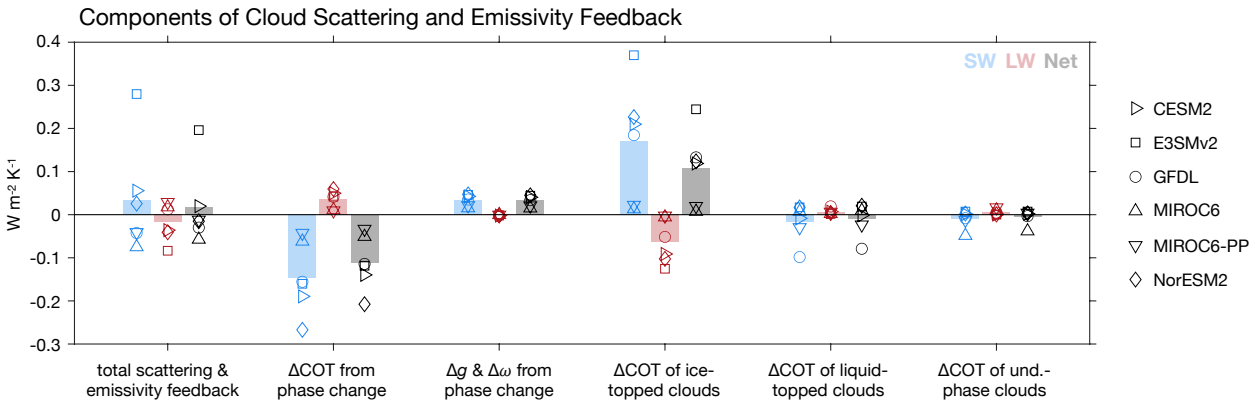

612

613 **Figure 10.** Global mean of the components of the cloud scattering and emissivity feedback. Markers show
614 individual models, and bars show the multi-model mean.

615

616 *b. Relative Importance of the Cloud Scattering and Emissivity Feedback caused by Phase Changes*

617 We now return to the main motivating question: Do cloud-phase changes cause a powerful
618 negative COT feedback at the global scale? The global mean of the overall net cloud feedback
619 ranges from 0.02 to 0.91 W m^{-2} K^{-1} and has a multi-model mean of 0.52 W m^{-2} K^{-1} (Fig. 11). The
620 goal is to determine how much of this feedback can be explained by changes in cloud scattering
621 and emissivity that arise from changes in cloud phase.

622 For an initial estimate, we assume that the scattering and emissivity feedback from cloud-
623 phase changes can be approximated by the feedback from changes in cloud-top phase ($\lambda_{tot,phase}$).
624 In other words, we neglect cases in which the phase changes in the interior of the cloud, but it
625 remains unchanged at cloud top. Outside of the polar regions, these cases are expected to occur in
626 deep and optically thick clouds that are not susceptible to substantial increases in albedo (Bodas-
627 Salcedo et al., 2016; Bodas-Salcedo, 2018). Thus, it is justified to neglect the feedback from phase
628 changes that occur exclusively in the cloud interior when estimating the global cloud scattering
629 and emissivity feedback from cloud-phase changes. The estimated net scattering and emissivity
630 feedback from cloud-phase changes ranges from -0.16 to -0.01 W m^{-2} K^{-1} and has a multi-model
631 mean of -0.08 W m^{-2} K^{-1} (Fig. 11). The multi-model mean of this feedback component is
632 approximately 15% of the magnitude of the multi-model mean of the overall cloud feedback (-
633 0.08 W m^{-2} K^{-1} vs. 0.52 W m^{-2} K^{-1}). The inter-model range of the cloud scattering and emissivity

feedback from cloud-top phase changes is also approximately six times smaller than the inter-model range of the overall cloud feedback, so cloud-top phase conversions do not explain much of the spread in feedbacks among models.

The estimated cloud scattering and emissivity feedback from phase conversions can be refined by adding a term that represents phase changes that occur exclusively in the cloud interior. As noted before, supercooled liquid-topped clouds become optically thicker in the polar regions in response to surface warming (Fig. 8e). We assume that this feedback is caused entirely by phase changes that occur in the interior of liquid-topped mixed-phase clouds. Other mechanisms may contribute to the negative COT feedback in polar liquid-topped clouds by enhancing condensation, so this calculation is best interpreted as an upper bound for the magnitude of the cloud scattering and emissivity feedback from cloud-phase conversions (Betts and Harshvardhan, 1987; Terai et al., 2019; McCoy et al., 2020; Frazer and Ming, 2022; McCoy et al., 2023). The COT feedback of supercooled liquid-topped clouds, $\lambda_{\Delta COT,sc\ liq}$, is estimated by integrating the COT feedback of liquid-topped clouds over the CTP bins in which the midpoint temperature is colder than 0 °C in the average annual cycle from the CTL simulations. Furthermore, we assume that the COT feedback of undetermined-phase clouds, $\lambda_{\Delta COT,und}$, is caused by changes in cloud-top phase that are not large enough to shift the phase category to liquid. $\lambda_{\Delta COT,sc\ liq}$ and $\lambda_{\Delta COT,und}$ are added to the feedback from cloud-top phase conversions to obtain a refined estimate of the scattering and emissivity feedback from cloud-phase changes, $\hat{\lambda}_{tot,phase}$:

$$\hat{\lambda}_{tot,phase} = \lambda_{tot,phase} + \lambda_{\Delta COT,sc\ liq} + \lambda_{\Delta COT,und}.$$

$\hat{\lambda}_{tot,phase}$ ranges from -0.17 to -0.02 W m^{-2} K^{-1} and has a multi-model mean of -0.10 W m^{-2} K^{-1} (Fig. 11). The multi-model mean of $\hat{\lambda}_{tot,phase}$ is approximately 19% of the magnitude of the multi-model mean of the overall cloud feedback (-0.10 W m^{-2} K^{-1} vs. 0.52 W m^{-2} K^{-1}). Thus, the initial and refined estimates both indicate that changes in cloud scattering and emissivity from cloud-phase conversions make a modest contribution to the overall cloud feedback at the global scale.

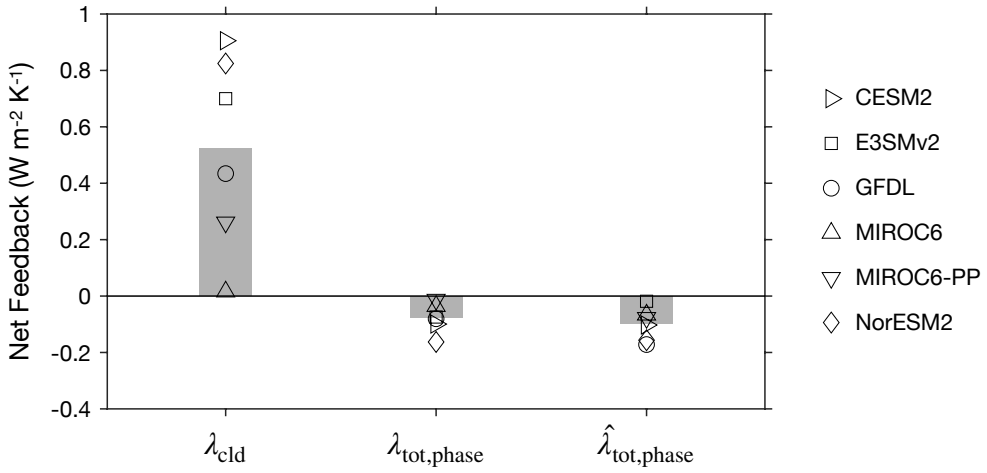

659

660 **Figure 11.** Comparison of the overall cloud feedback and the cloud scattering and emissivity feedback from
661 cloud-phase changes. λ_{cld} is the overall cloud feedback. $\lambda_{tot,phase}$ is the scattering and emissivity feedback from
662 changes in cloud-top phase. $\hat{\lambda}_{tot,phase}$ is similar to $\lambda_{tot,phase}$ except that it includes an additional term that
663 represents phase changes that occur exclusively in the cloud interior. Markers show individual models, and bars
664 show the multi-model mean. All values represent the global-mean net radiative feedback.
665

666 **4. Discussion**

667 Our findings contribute to a body of literature about the COT feedback from cloud-phase
668 changes simulated by GCMs. Some studies have argued that this is a powerful feedback
669 mechanism that may control the sign of the overall cloud feedback simulated by some GCMs,
670 while others have argued that it is less important (Li and Le Treut, 1991; Storelvmo et al., 2015;
671 Lohmann and Neubauer, 2018; Bodas-Salcedo, 2018). Perhaps the most compelling evidence for
672 a strong cloud-phase feedback comes from GCM experiments in which model parameters are
673 perturbed to vary the cloud-phase partitioning in the mean climate state (Choi et al., 2014; McCoy
674 et al., 2016; Tan et al., 2016; Frey and Kay, 2018; Hofer et al., 2024). A suite of experiments is
675 performed with different phase partitioning, and variations in the overall cloud feedback across
676 the experiments are interpreted as evidence for the strength of the cloud-phase feedback. Although
677 this approach has provided some of the most direct evidence of the cloud-phase feedback, it has
678 two important limitations. First, the act of changing model parameters may change other cloud-
679 feedback mechanisms in addition to the cloud-phase feedback, but it has not been possible to
680 identify and remove these potential confounding factors. Second, GCMs from different model

681 families typically represent cloud physics with structurally different parameterizations, so results
682 from perturbed-parameter experiments are specific to individual GCMs. For these reasons,
683 perturbed-parameter studies do not rule out the possibility that the cloud-phase feedback is
684 relatively weak. The method developed here overcomes these limitations by quantifying the cloud
685 scattering and emissivity feedback from phase changes in a diverse ensemble of GCMs while
686 avoiding confounding factors. Our results indicate that changes in cloud scattering and emissivity
687 from phase conversions cause a global net radiative feedback between -0.17 and -0.01 W m^{-2} K^{-1}
688 (Fig. 11). Considering all of the evidence, we believe that changes in cloud scattering and
689 emissivity from phase conversions make a modest contribution to overall cloud feedback at the
690 global scale.

691 Although it is not a focus of this study, another notable finding is the existence of a positive
692 feedback from optical thinning of ice-topped clouds in the tropical upper troposphere (Fig. 8d).
693 One possible explanation is that surface warming weakens the tropical overturning circulation and
694 disproportionately reduces the amount of optically thick ice clouds (Jeevanjee, 2022; Sokol et al.,
695 2024). Indeed, five out of the six GCMs predict that ice-topped clouds in the tropical upper
696 troposphere will shrink in amount in response to surface warming, and all models predict that the
697 proportion of ice-topped clouds that are optically thin will increase (Fig. C1). These results suggest
698 that weakening of the tropical overturning circulation may contribute to the optical thinning of ice-
699 topped clouds simulated by the GCMs. However, our method probably exaggerates the magnitude
700 of the ice-cloud COT feedback due to confounding factors from vertical shifts in clouds (Appendix
701 C). The ice-cloud COT feedback estimated here should thus be interpreted with caution. More
702 work is needed to understand and quantify this feedback given its importance for climate
703 sensitivity (Sherwood et al., 2020; Raghuraman et al., 2024; Dawson and Schiro, 2024).

704 Finally, the methods and model diagnostics developed here may have applications beyond
705 studying the cloud-phase feedback. Ice, liquid, and mixed-phase clouds exhibit different radiative
706 feedback and adjustment mechanisms in response to external perturbations, so cloud-top phase is
707 a natural partitioning metric to gain insight into the importance of different mechanisms (Duran et
708 al., 2024). Code to compute the MODIS histograms in GCM simulations is now included in the
709 COSPv2.0 open-source software package, and the cloud radiative kernels are publicly available
710 online (CFMIP, 2024; Wall, 2024a). Equivalent histograms from real satellite observations are

711 also included in the MODIS MCD06COSP dataset (Pincus et al., 2023). These resources could
712 facilitate new opportunities for quantifying cloud feedbacks and adjustments, evaluating models,
713 and relating observable quantities to feedbacks simulated by GCMs.

714 **5. Conclusion**

715 Radiative feedbacks from changes in COT are considered to be a major source of inter-
716 model spread in GCM projections of anthropogenic climate change (Zelinka et al., 2020). Thus, a
717 key goal is to understand the relative importance of the underlying mechanisms. One leading
718 hypothesis is that cloud-phase changes cause clouds to optically thicken, producing a major
719 negative feedback (Storelvmo et al., 2015). However, there has not been a framework to rigorously
720 quantify this feedback, so its importance relative to other mechanisms has been unclear (cf. Tan et
721 al., 2016; Lohmann and Neubauer, 2018).

722 We address this challenge by developing a method to quantify the feedback from changes
723 in cloud scattering properties and emissivity that arise from changes in cloud-top phase. This
724 feedback component is dominated by changes in COT, but it also includes a smaller term from
725 changes in cloud single-scattering properties (g and ω). The method is applied to six CMIP6-era
726 GCMs run with prescribed sea-surface temperature to investigate the contribution of cloud-phase
727 changes to the overall cloud feedback. The global mean of the net cloud scattering and emissivity
728 feedback from cloud-phase changes ranges from -0.17 to -0.01 W m^{-2} K^{-1}, while the overall net
729 cloud feedback ranges from 0.02 to 0.91 W m^{-2} K^{-1} (Fig. 11). The multi-model mean of the cloud
730 scattering and emissivity feedback from cloud-phase changes is approximately 19% of the
731 magnitude of the multi-model mean of the overall cloud feedback. Thus, changes in cloud
732 scattering properties and emissivity from phase conversions cause a robust negative feedback that
733 makes a modest contribution to the overall cloud feedback at the global scale.

734 Although our findings clarify how phase conversions change cloud scattering and
735 emissivity, they do not quantify the extent to which phase conversions change cloud amount. Phase
736 conversions that replace ice-containing clouds with pure-liquid clouds are expected to reduce the
737 precipitation efficiency (Lutsko and Cronin, 2018). This, in turn, may extend cloud lifetimes and
738 increase the cloud amount (Mülmenstädt et al., 2021). Quantifying this feedback component is an
739 important next step for understanding the role of cloud-phase conversions in global climate
740 change.
741

Acknowledgments.

We thank Joel Norris, Robert Pincus, and Steve Klein for helpful comments that improved this study. CJW received funding from the European Union's Horizon 2020 research and innovation programme under the Marie Skłodowska-Curie grant agreement No 101019911. CJW, DP, NJL, and MZ acknowledge the support of NOAA MAPP award NA20OAR4310387. MLD and BM acknowledge the support of NOAA MAPP award NA20OAR4310392. BM also acknowledges support by the U.S. Department of Energy, Office of Science, Office of Biological & Environmental Research, Regional and Global Model Analysis component of the Earth and Environmental System Modeling Program under Award Number DE-SC0022070 and National Science Foundation (NSF) IA 1947282. PLM and YQ acknowledge support from U.S. Department of Energy, Office of Science, Office of Biological & Environmental Research, Regional and Global Model Analysis program area. The Pacific Northwest National Laboratory (PNNL) is operated for the DOE by the Battelle Memorial Institute under Contract DE-AC05-76RL01830. MD and TS acknowledge funding from the European Union's Horizon Europe research and innovation programme under the ERC Consolidator grant agreement No 101045273. TM was supported by the JST FOREST Program (Grant JPMJFR206Y); the Japan Society for the Promotion of Science KAKENHI (Grant JP23K13171); the Environment Research and Technology Development Fund (Grant JPMEERF21S12004) of the Environmental Restoration and Conservation Agency, provided by the Ministry of Environment of Japan; and the Advanced Studies of Climate Change Projection (SENTAN) of the Ministry of Education, Culture, Sports, Science, and Technology (Grant JPMXD0722680395). MIROC numerical simulations were executed with the SX-Aurora TSUBASA supercomputer system of the National Institute for Environmental Studies, Japan. This material is based upon work supported by the National Center for Atmospheric Research, which is a major facility sponsored by the National Science Foundation under Cooperative Agreement No. 1852977. We would like to acknowledge high-performance computing support from Derecho (doi:10.5065/QX9A-PG09) provided by NCAR's Computational and Information Systems Laboratory, sponsored by the National Science Foundation.

Data Availability Statement.

Code to produce the MODIS cloud histograms has been added to the open-source COSPv2.0 software package for GCMs and is publicly available online (CFMIP, 2024). GCM

773 output and the radiative kernels developed in this study are also publicly available online (Wall,
774 2024a; Wall, 2024b).

APPENDIX

Appendix A: Validation of the Cloud Radiative Kernel Method against GCM Radiative Transfer Schemes

CRE is defined as the clear-sky upward radiative flux at the top of the atmosphere, R_{clr}, minus the all-sky upward radiative flux at the top of the atmosphere, R_{all}. The all-sky flux can be expressed as

$$R_{\mathrm{all}} = \frac{1}{100\%}[R_{\mathrm{cld}}C_{\mathrm{tot}} + R_{\mathrm{clr}}(100\% - C_{\mathrm{tot}})]$$

where R_{cld} is the upward radiative flux at the top of the atmosphere averaged over the cloud-covered portion of the domain. Substituting this relation into the definition of CRE and differentiating yields

$$CRE' \approx \frac{1}{100\%}[C_{tot}^{'}(\bar{R}_{clr} - \bar{R}_{cld}) - \bar{C}_{tot}R'_{cld}] + \frac{1}{100\%}\bar{C}_{tot}R'_{clr} \qquad \text{(A1)}$$

where primes denote anomalies relative to the climatological annual cycle. The first term on the right side represents the component of the anomalous CRE that is attributable to cloud anomalies with non-cloud factors fixed. This term can be predicted by the cloud-radiative-kernel method. The second term on the right side represents the component of the anomalous CRE that is attributable to clear-sky radiative flux anomalies with clouds fixed.

We validate the kernel method based on its ability to predict monthly CRE anomalies that arise from natural variability in the CTL simulations. For each latitude-longitude grid-box, the average annual cycle is removed from all variables, and the anomalous CRE predicted by the kernel method, $\mathrm{CRE}'_{\mathrm{kernel}}$, is computed as

$$\mathrm{CRE}'_{\mathrm{kernel}} = \sum_{p=1}^{7}\sum_{t=1}^{7}\sum_{i=1}^{3} C'_{pti}K_{pti} + \frac{1}{100\%}\bar{C}_{\mathrm{tot}}R'_{\mathrm{clr}}.$$

$\mathrm{CRE}'_{\mathrm{kernel}}$ is compared with the corresponding CRE anomalies from the GCM output, $\mathrm{CRE}'_{\mathrm{GCM}}$. The comparison is restricted to the ice-free global ocean to minimize the magnitude of the anomalous clear-sky radiative flux term on the right side of Eq. (A1). For each model, we combine the data from all latitude-longitude-month grid-boxes and relate $\mathrm{CRE}'_{\mathrm{kernel}}$ to $\mathrm{CRE}'_{\mathrm{GCM}}$ using ordinary least-squares linear regression (Fig. A1). The squared coefficient of determination is at

least 0.95 for SW CRE and at least 0.87 for LW CRE for the six GCMs, indicating a strong linear relationship. Thus, bias in CRE predicted by the kernel method can be estimated as $(m-1)\times 100\%$, where m is the linear regression slope. The biases in SW CRE, LW CRE, and net CRE averaged across the six CGMs are +14%, -8%, and +5%, respectively. The biases range from +10% to +20% for SW CRE, -18% to -1% for LW CRE, and -1% to +17% for net CRE (Fig. A1). These values are comparable to biases estimated in previous cloud-radiative-kernel analyses (Zhou et al., 2013; Ceppi and Gregory, 2017; Wall et al., 2022). Thus, the kernel method is consistent with the radiative transfer models in the GCMs to within a typical degree of accuracy.

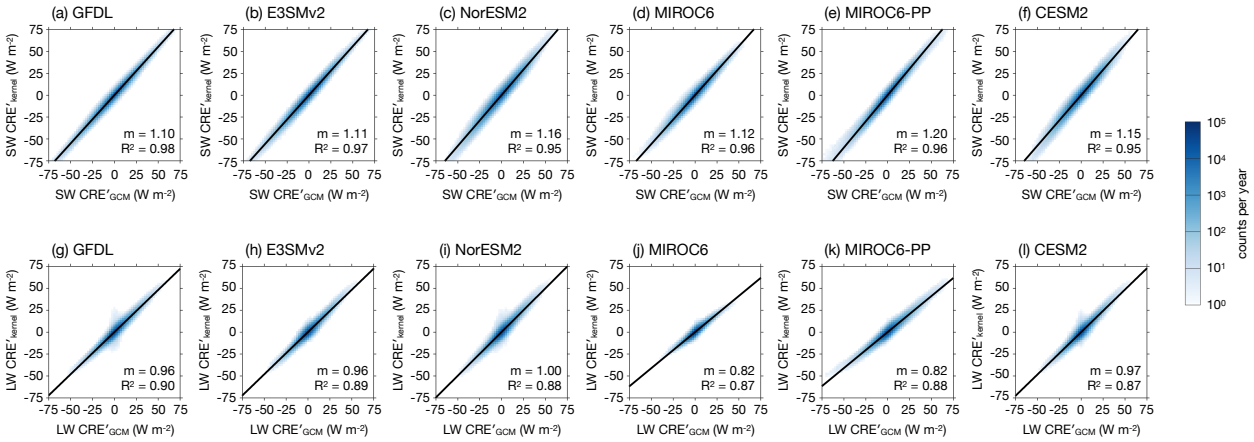

Figure A1. Validation of the cloud radiative kernel method based on its ability to predict CRE anomalies from natural variability in the CTL simulations. (a-f) Validation of SW CRE for GFDL, E3SMv2, NorESM2, MIROC6, MIROC6-PP, and CESM2, respectively. The anomalous CRE predicted by the kernel method ($\mathrm{CRE'_{kernel}}$) is plotted as a function of the anomalous CRE from the GCM output ($\mathrm{CRE'_{GCM}}$). Joint histograms are compiled from all latitude-longitude-month grid-boxes over the ice-free global ocean. Blue shading shows counts per simulation year with a logarithmic color scale, and the black line shows the least-squares ordinary linear regression fit. The regression slope (m) and squared coefficient of determination (R^2) are printed on each panel. (g-l) Similar to (a-f), but for LW CRE.

Appendix B: Comparison with other Cloud-Feedback Decompositions

Our method decomposes the cloud feedback into the six terms in Eq. (5) at each CTP bin. This differs from conventional cloud-feedback decompositions, which have much coarser CTP resolution or do not resolve feedback components by CTP at all (Taylor et al., 2007; Zelinka et al., 2012b; Zelinka et al., 2013). For example, Zelinka et al. (2016; hereafter Z16) decomposed

feedbacks for low clouds and non-low clouds, defined by CTP ≥ 680 hPa and CTP < 680 hPa, respectively. They partitioned the cloud feedback in each of these CTP intervals into components from changes in cloud amount, cloud altitude, and COT. We quantify the impact of the different CTP resolution by comparing our feedback decomposition with that of Z16. For the Z16-based estimates, a radiative kernel is computed following their method, and feedbacks are diagnosed using a MODIS CTP-COT joint histogram for clouds of all phases. This ensures that differences in the estimated feedback components are caused by differences in the mathematical framework rather than differences in the input data (Section 2d). Low- and non-low-cloud feedbacks are calculated with the method of Z16, and the corresponding feedbacks are calculated with our method by vertically integrating the terms in Eq. (5) over the pressure intervals given by CTP ≥ 680 hPa and CTP < 680 hPa. Finally, the cloud amount and altitude feedbacks from the Z16 decomposition are combined because our method cannot separate these terms (Section 2c). The feedback estimates for low- and non-low clouds from the two methods are then directly comparable to one another.

The global-mean net radiative feedback for non-low clouds agrees very well between the two methods, but the partitioning into components differs slightly (Fig. B1a-c). The Z16 method estimates a more-positive feedback from changes in cloud amount and altitude, and it estimates a less-positive or more-negative feedback from changes in COT. These differences are approximately +0.09 W m^{-2} K^{-1} and -0.07 W m^{-2} K^{-1} averaged across the six GCMs, respectively (Z16 method minus our method). Furthermore, the two methods partition low-cloud feedbacks very similarly because these clouds occupy only two CTP bins of the MODIS histogram (Fig. B1d-f). Thus, our feedback decomposition agrees reasonably well with the conventional decomposition of Z16, albeit with some differences for non-low clouds. A thorough discussion of how the cloud-feedback decomposition depends on the CTP intervals chosen in the analysis can be found in Z16.

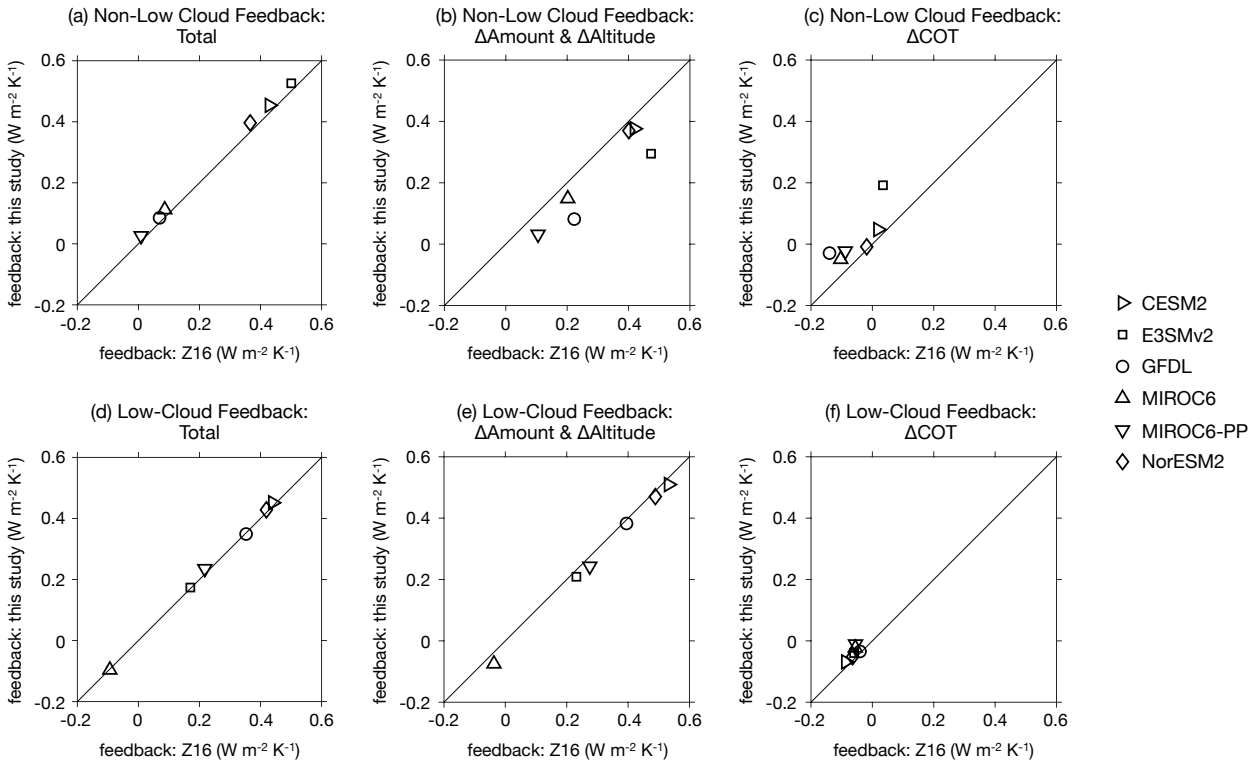

Figure B1. Comparison of the feedback decomposition methods of this study and Zelinka et al. (2016) (Z16). (a) Scatterplot of total feedback from non-low clouds computed with the two methods. Points show global-mean net radiative feedbacks from the six GCMs, and the diagonal shows the one-to-one line. (b-c) Similar to (a), but showing the feedback component from changes in the amount and altitude of non-low clouds and the feedback component from changes in the COT of non-low clouds, respectively. (d-f) Similar to (a-c), but for low clouds. Non-low clouds and low clouds are defined by CTP < 680 hPa and CTP ≥ 680 hPa, respectively.

Appendix C: The COT Feedback of Tropical Ice-Topped Clouds

A notable result of our analysis is a positive feedback from optical thinning of ice-topped clouds in the tropical upper troposphere (Fig. 8d). One possible explanation for this feedback is that surface warming weakens the tropical overturning circulation (Jeevanjee, 2022). This is expected to disproportionately reduce the amount of optically thick and intermediate ice clouds detrained from deep convection, thereby causing the overall ice-cloud population to become optically thinner (Sokol et al., 2024). Indeed, the simulated changes in tropical ice-topped clouds are qualitatively consistent with this mechanism (Fig. C1).

Another possible contributing factor to the estimated ice-cloud COT feedback is associated with rising cloud tops. As the surface warms, the highest ice-topped clouds shift upward,

potentially changing the COT distribution at different pressure levels (Hartmann and Larson, 2002). For instance, consider the CTP interval between 0 hPa and 180 hPa. The strongest and deepest convection will detrain clouds into this pressure interval in the CTL simulation. However, as the atmosphere warms and clouds shift upward, weaker convection may detrain clouds into the interval as well. The introduction of weaker convection could change the COT distribution in the CTP interval between 0 hPa and 180 hPa and thereby contribute to the estimated COT feedback. However, this would be better interpreted as part of the cloud-altitude feedback. To check for evidence of this confounding factor, we perform two sensitivity tests in which the CTP bins in the upper troposphere are merged prior to the feedback analysis. In one test the CTP bins between 180 hPa and 440 hPa are merged, and in a second test the CTP bins between 0 hPa and 310 hPa are merged. The coarsening of the CTP bins reduces the magnitude of the estimated ice-cloud COT feedback, and in two cases it even changes the sign (Fig. C2). This indicates that vertical shifts in ice-topped clouds probably act as a confounding factor that exaggerates the magnitude of the estimated ice-cloud COT feedback. This confounding factor could affect the estimated ice-cloud COT feedback in the extratropics as well. Thus, this feedback component should be interpreted with caution.

This limitation is a consequence of the fact that cloud feedbacks are decomposed separately for each CTP bin. A common alternative choice is to first group all non-low clouds (CTP < 680 hPa) and then compute the feedback from changes in their COT distribution (Zelinka et al., 2016). This approach avoids confounding factors in the estimated ice-cloud COT feedback from vertical shifts in clouds. However, it has the disadvantage that changes in upper-tropospheric ice-topped clouds and mid-tropospheric liquid-topped clouds could contribute to the estimated cloud-phase feedback, even though these changes happen at different pressure levels and are not caused by one phase replacing the other. We chose to quantify cloud feedbacks separately for each CTP bin to quantify the cloud-phase feedback as accurately as possible. A more refined decomposition method will be needed to separate the radiative feedbacks from changes in the amount, altitude, and COT of upper-tropospheric ice clouds.

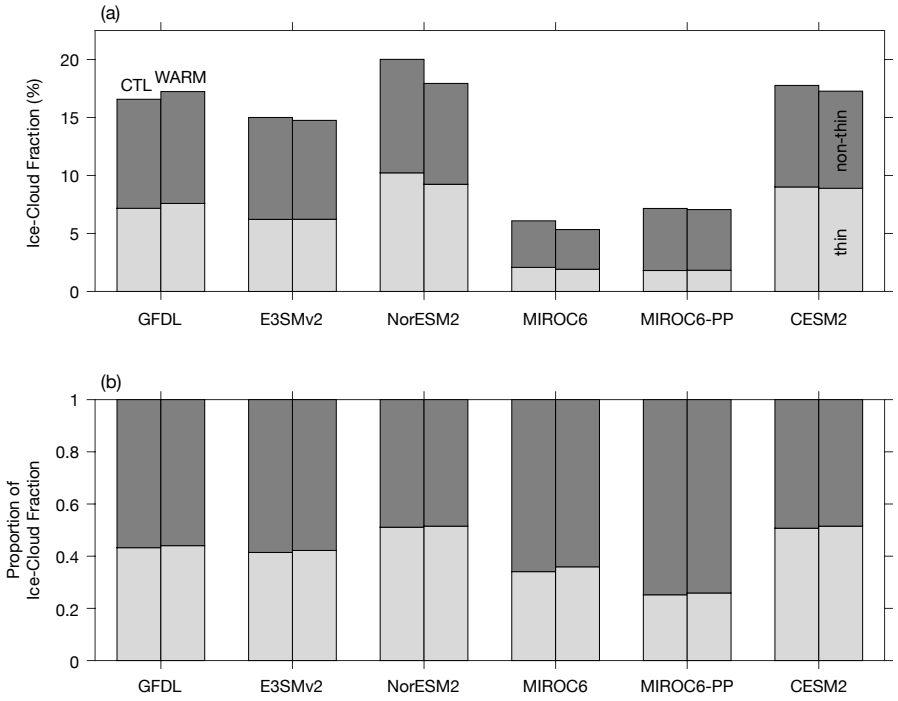

894

895 **Figure C1.** Fraction of tropical ice-topped clouds partitioned by COT. (a) Mean fraction of thin and non-thin
896 ice clouds, defined by $0.3 \leq \text{COT} < 3.6$ and $\text{COT} \geq 3.6$, respectively. The ice-cloud fraction is computed over
897 clouds with CTP < 310 hPa, and it is averaged over the seasonal cycle and between 30°S and 30°N. The CTL
898 and WARM simulations are shown by adjacent bars. Thin and non-thin clouds are shown with light gray and
899 dark gray colors, respectively. (b) Similar to (a) but showing the proportion of ice-cloud fraction in the thin and
900 non-thin categories.

901

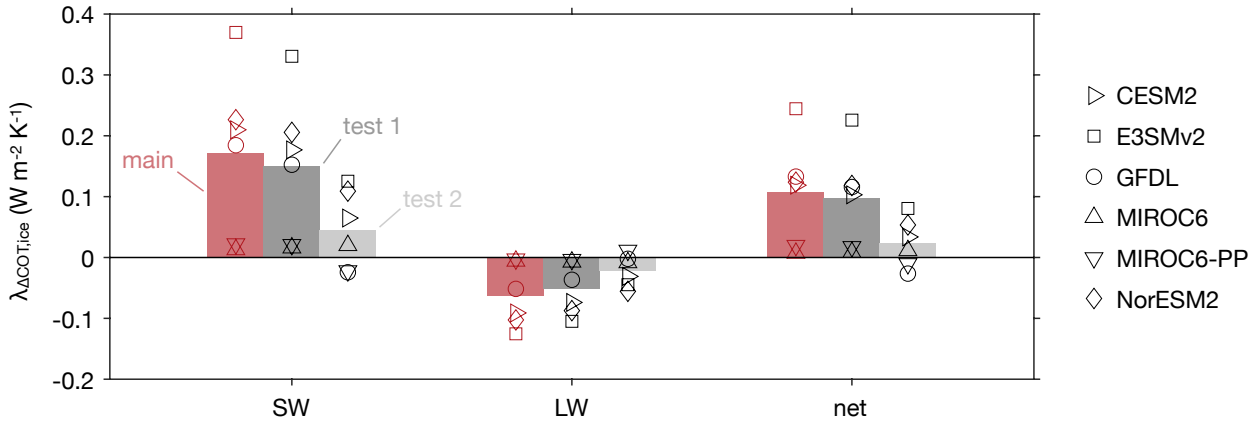

902

903 **Figure C2.** Sensitivity tests for the COT feedback from ice-topped clouds ($\lambda_{\Delta COT,ice}$) in the tropics. "Main"
904 shows the feedback estimates presented in the main text. "Test 1" is a sensitivity test in which the CTP bins

between 180 hPa and 440 hPa are merged prior to computing feedbacks. “Test 2” is similar to “Test 1” except that the CTP bins between 0 hPa and 310 hPa are merged. Feedbacks are averaged between 30°S and 30°N.

907 REFERENCES

908 Betts, A. K., & Harshvardhan. (1987). Thermodynamic Constraint on the Cloud Liquid Water
909 Feedback in Climate Models. *J. Geophys. Res.*, *92*(6), 8483–8485.

910 Bjordal, J., Storelvmo, T., Alterskjær, K., and Carlsen, T., 2020: Equilibrium climate sensitivity
911 above 5 °C plausible due to state-dependent cloud feedback. *Nat. Geosci.*, *13*(11), 718–721.
912 https://doi.org/10.1038/s41561-020-00649-1

913 Bodas-Salcedo, A., and Coauthors, 2011: COSP: Satellite simulation software for model
914 assessment. *Bull. Am. Meteorol. Soc.*, *92*(8), 1023–1043.
915 https://doi.org/10.1175/2011BAMS2856.1

916 Bodas-Salcedo, A., Andrews, T., Karmalkar, A. V., and Ringer, M. A., 2016: Cloud liquid water
917 path and radiative feedbacks over the Southern Ocean. *Geophy. Res. Lett.*, *43*(20), 10,938-
918 10,946. https://doi.org/10.1002/2016GL070770

919 Bodas-Salcedo, A., 2018: Cloud Condensate and Radiative Feedbacks at Midlatitudes in an
920 Aquaplanet. *Geophys. Res. Lett.*, *45*(8), 3635–3643. https://doi.org/10.1002/2018GL077217

921 Ceppi, P., Brient, F., Zelinka, M. D., and Hartmann, D. L., 2017: Cloud feedback mechanisms and
922 their representation in global climate models. *WIREs Clim. Change*, 8:
923 e465. https://doi.org/10.1002/wcc.465

924 Ceppi, P., and Gregory, J. M., 2017: Relationship of tropospheric stability to climate sensitivity
925 and Earth's observed radiation budget. *Proc. Natl. Acad. Sci. U.S.A.*, *114*(50), 13126–13131.
926 https://doi.org/10.1073/pnas.1714308114

927 Ceppi, P., Hartmann, D. L., and Webb, M. J., 2016: Mechanisms of the Negative Shortwave Cloud
928 Feedback in Middle to High Latitudes. *J. Clim.*, 29, 139-157, https://doi.org/10.1175/JCLI-D-
929 15-0327.1.

930 CFMIP, 2024: COSPv2.0 MODIS Simulator. Accessed 2 July 2024,
931 https://github.com/CFMIP/COSPv2.0/tree/master/src/simulator/MODIS_simulator

932 Chao, L.-W., Zelinka, M. D., and Dessler, A. E., 2024: Evaluating cloud feedback components in
933 observations and their representation in climate models. *J. Geophys. Res. Atmos.*, 129,
934 e2023JD039427. https://doi.org/10.1029/2023JD039427

935 Choi, Y.-S., Ho, C.-H., Park, C.-E., Storelvmo, T., and Tan, I., 2014: Influence of cloud phase
936 composition on climate feedbacks, *J. Geophys. Res. Atmos.*, 119, 3687–3700, doi:10.1002/
937 2013JD020582.

938 Clough, S. A., and Coauthors, 2005: Atmospheric radiative transfer modeling: A summary of the
939 AER codes. *J. Quant. Spectrosc. Radiat. Transfer*, *91*(2), 233–244.
940 https://doi.org/10.1016/j.jqsrt.2004.05.058

941 Danabasoglu, G., and Coauthors, 2020: The Community Earth System Model Version 2 (CESM2).
942 *J. Adv. Model. Earth Syst.*, *12*(2), 1–35. https://doi.org/10.1029/2019MS001916

943 Davis, I., and Medeiros, B., 2024: Assessing CESM2 Clouds and Their Response to Climate
944 Change Using Cloud Regimes. *J. Clim.*, 37, 2965–2985, https://doi.org/10.1175/JCLI-D-23-
945 0337.1.

946 Dawson, E., and K. A. Schiro, 2024: Tropical High Cloud Feedback Relationships to Climate
947 Sensitivity. *J. Clim.*, 38, 583–596, https://doi.org/10.1175/JCLI-D-24-0218.1.

948 Debolskiy, M. D., 2024: Release release-noresm2.1.1-cosp2-update mvdebolskiy/NorESM.
949 GitHub. https://github.com/mvdebolskiy/NorESM/releases/tag/release-noresm2.1.1-cosp2-
950 update

951 Donner, L. J., and Coauthors, 2011: The dynamical core, physical parameterizations, and basic
952 simulation characteristics of the atmospheric component AM3 of the GFDL global coupled
953 model CM3. *J. Clim.*, *24*(13), 3484–3519. https://doi.org/10.1175/2011JCLI3955.1

954 Duffy, M. L., Medeiros, B., Gettelman, A., and Eidhammer, T., 2024: Perturbing Parameters to
955 Understand Cloud Contributions to Climate Change. *J. Clim.*, *37*(1), 213–227.
956 https://doi.org/10.1175/JCLI-D-23-0250.1

957 Duran, B. M., and Coauthors, 2024: A new method for diagnosing effective radiative forcing from
958 aerosol-cloud interactions in climate models, *Atmos. Chem. Phys.* (in press),
959 https://doi.org/10.5194/egusphere-2024-3063

960 Forster, P., and Coauthors, 2021: The Earth's Energy Budget, Climate Feedbacks, and Climate
961 Sensitivity. In Climate Change 2021: The Physical Science Basis. Contribution of Working
962 Group I to the Sixth Assessment Report of the Intergovernmental Panel on Climate Change
963 [Masson-Delmotte, V., P. Zhai, A. Pirani, S.L. Connors, C. Péan, S. Berger, N. Caud, Y. Chen,

L. Goldfarb, M.I. Gomis, M. Huang, K. Leitzell, E. Lonnoy, J.B.R. Matthews, T.K. Maycock, T. Waterfield, O. Yelekçi, R. Yu, and B. Zhou (eds.)]. Cambridge University Press, Cambridge, United Kingdom and New York, NY, USA, pp. 923–1054, doi:10.1017/9781009157896.009.

Frazer, M. E., and Ming, Y., 2022: Understanding the Extratropical Liquid Water Path Feedback in Mixed-Phase Clouds with an Idealized Global Climate Model. *J. Clim.*, *35*(8), 2391–2406. https://doi.org/10.1175/JCLI-D-21-0334.1

Frey, W. R., and Kay, J. E., 2018: The influence of extratropical cloud phase and amount feedbacks on climate sensitivity. *Clim. Dyn.*, *50*(7–8), 3097–3116. https://doi.org/10.1007/s00382-017-3796-5

Fu, Q., 1996: An Accurate Parameterization of the Solar Radiative Properties of Cirrus Clouds for Climate Models. *J. Clim.*, 9, 2058–2082, https://doi.org/10.1175/1520-0442(1996)009<2058:AAPOTS>2.0.CO;2.

Golaz, J. C., and Coauthors, 2022: The DOE E3SM Model Version 2: Overview of the Physical Model and Initial Model Evaluation. *J. Adv. Model. Earth Syst.*, *14*(12), 1–51. https://doi.org/10.1029/2022MS003156

Griffies, S. M., and Coauthors, 2011: The GFDL CM3 coupled climate model: Characteristics of the ocean and sea ice simulations. *J. Clim.*, *24*(13), 3520–3544. https://doi.org/10.1175/2011JCLI3964.1

Hartmann, D. L., and Larson, K., 2002: An important constraint on tropical cloud - climate feedback. *Geophys. Res. Lett.*, *29*(20), 10–13. https://doi.org/10.1029/2002GL015835

Hirota, N., Michibata, T., Shiogama, H., Ogura, T., and Suzuki, K., 2022: Impacts of precipitation modeling on cloud feedback in MIROC6. *Geophys. Res. Lett.*, 49, e2021GL096523.https://doi.org/10.1029/2021GL096523

Hofer, S., and Coauthors, 2024: Realistic representation of mixed-phase clouds increases projected climate warming. *Commun. Earth Environ.*, 5, 390. https://doi.org/10.1038/s43247-024-01524-2

Jeevanjee, N. (2022). Three rules for the decrease of tropical convection with global warming. *J. Adv. Model. Earth Syst.*, 14, e2022MS003285. https://doi.org/10.1029/2022MS003285

Kuma, P., Bender, F. A. M., and Jönsson, A. R., 2023: Climate Model Code Genealogy and Its Relation to Climate Feedbacks and Sensitivity. *J. Adv. Model. Earth Syst.*, *15*(7), 1–19. https://doi.org/10.1029/2022MS003588

Li, Z. X., and Le Treut, H., 1992: Cloud-radiation feedbacks in a general circulation model and their dependence on cloud modelling assumptions. *Clim. Dyn.*, 7, 133–139. https://doi.org/10.1007/BF00211155

Lohmann, U., and Neubauer, D., 2018: The importance of mixed-phase and ice clouds for climate sensitivity in the global aerosol-climate model ECHAM6-HAM2. *Atmos. Chem. Phys.*, *18*(12), 8807–8828. https://doi.org/10.5194/acp-18-8807-2018

Lutsko, N. J. and Cronin, T. W., 2018: Increase in precipitation efficiency with surface warming in radiative-convective equilibrium. *J. Adv. Model. Earth Syst.*, 10, 2992–3010. https://doi.org/10.1029/2018MS001482

McCoy, D. T., Field, P., Bodas-Salcedo, A., Elsaesser, G. S., and Zelinka, M. D., 2020: A regime-oriented approach to observationally constraining extratropical shortwave cloud Feedbacks. *J. Clim.*, *33*(23), 9967–9983. https://doi.org/10.1175/JCLI-D-19-0987.1

McCoy, D. T., Frazer, M. E., Mülmenstädt, J., Tan, I., Terai, C. R., and Zelinka, M. D., 2023: Extratropical Cloud Feedbacks. *Clouds and Their Climatic Impacts: Radiation, Circulation, and Precipitation*. S. C. Sullivan and C. Hoose, Ed., 133–157. https://doi.org/10.1002/9781119700357.ch6

McCoy, D. T., Hartmann, D. L., Zelinka, M. D., Ceppi, P., and Grosvenor, D. P., 2015: Mixed-phase cloud physics and Southern Ocean cloud feedback in climate models, *J. Geophys. Res. Atmos.*, 120,9539–9554, doi:10.1002/2015JD023603.

McCoy, D. T., Tan, I., Hartmann, D. L., Zelinka, M. D., and Storelvmo, T., 2016: On the relationships among cloud cover, mixed-phase partitioning, and planetary albedo in GCMs. *J. Adv. Model. Earth Syst.*, 8, 650–668, doi:10.1002/2015MS000589.

Medeiros, B., Shaw, J., Kay, J. E., and Davis, I., 2023: Assessing clouds using satellite observations through three generations of global atmosphere models. *Earth Space Sci.*, 10, e2023EA002918. https://doi.org/10.1029/2023EA002918

Michibata, T., Suzuki, K., Sekiguchi, M., and Takemura, T., 2019: Prognostic Precipitation in the MIROC6-SPRINTARS GCM: Description and Evaluation Against Satellite Observations. *J. Adv. Model. Earth Syst.*, *11*(3), 839–860. https://doi.org/10.1029/2018MS001596

Mitchell, J. F. B., Senior, C. A., and Ingram, W. J., 1989: CO_2 and climate: a missing feedback? *Nature*, *341*(September), 132–134.

Mülmenstädt, J., and Coauthors, 2021: An underestimated negative cloud feedback from cloud lifetime changes. *Nat. Clim. Change*, *11*(6), 508–513. https://doi.org/10.1038/s41558-021-01038-1

Olivié, D., 2024: Release of NorESM2.1 – results from longer simulations. NorESM Documentation Pages, Accessed 27 July 2024, https://noresm-docs.readthedocs.io/en/noresm2.1/noresm2.1/noresm2.1_test_runs.html

Paynter, D., Frölicher, T. L., Horowitz, L. W., and Silvers, L. G., 2018: Equilibrium Climate Sensitivity Obtained From Multimillennial Runs of Two GFDL Climate Models. *J. Geophys. Res. Atmos.*, *123*(4), 1921–1941. https://doi.org/10.1002/2017JD027885

Pincus, R., and Coauthors, 2023: Updated observations of clouds by MODIS for global model assessment. *Earth Syst. Sci. Data*, *15*(6), 2483–2497. https://doi.org/10.5194/essd-15-2483-2023

Pincus, R., Platnick, S., Ackerman, S. A., Hemler, R. S., and Patrick Hofmann, R. J., 2012: Reconciling simulated and observed views of clouds: MODIS, ISCCP, and the limits of

instrument simulators. *J. Clim.*, *25*(13), 4699–4720. https://doi.org/10.1175/JCLI-D-11-00267.1

Qin, Y., Zelinka, M. D., and Klein, S. A., 2022: On the Correspondence Between Atmosphere-Only and Coupled Simulations for Radiative Feedbacks and Forcing From CO2. *J. Geophys. Res. Atmos.*, *127*(3), 1–21. https://doi.org/10.1029/2021JD035460

Qin, Y., and Coauthors, 2024: Causes of reduced climate sensitivity in E3SM from version 1 to version 2. *J. Adv. Model. Earth Syst.*, 16, e2023MS003875. https://doi.org/10.1029/2023MS003875

Raghuraman, S. P., Medeiros, B., & Gettelman, A., 2024: Observational quantification of tropical high cloud changes and feedbacks. *J. Geophys. Res. Atmos.*, 129, e2023JD039364. https://doi.org/10.1029/2023JD039364

Seland, Ø., and Coauthors, 2020: Overview of the Norwegian Earth System Model (NorESM2) and key climate response of CMIP6 DECK, historical, and scenario simulations. *Geosci. Model Dev.,* 13. https://doi.org/10.5194/gmd-13-6165-2020

Sherwood, S. C., and Coauthors, 2020: An Assessment of Earth's Climate Sensitivity Using Multiple Lines of Evidence. *Rev. Geophys.*, *58*(4), 1–92. https://doi.org/10.1029/2019RG000678

Slingo, A., 1989: A GCM Parameterization for the Shortwave Radiative Properties of Water Clouds. *J. Atmos. Sci.*, 46, 1419–1427, https://doi.org/10.1175/1520-0469(1989)046<1419:AGPFTS>2.0.CO;2.

Sokol, A. B., Wall, C. J., and Hartmann, D. L., 2024: Greater climate sensitivity implied by anvil cloud thinning. *Nat. Geosci.* 17, 398–403. https://doi.org/10.1038/s41561-024-01420-6

Storelvmo, T., Tan, I., and Korolev, A. V., 2015: Cloud Phase Changes Induced by CO_2 Warming – a Powerful yet Poorly Constrained Cloud-Climate Feedback. *Curr. Clim. Change Rep.*, *1*(4), 288–296. https://doi.org/10.1007/s40641-015-0026-2

Tan, I., Oreopoulos, L., and Cho, N., 2019: The Role of Thermodynamic Phase Shifts in Cloud Optical Depth Variations With Temperature. *Geophys. Res. Lett.*, *46*(8), 4502–4511. https://doi.org/10.1029/2018GL081590

Tan, I., Storelvmo, T., and Zelinka, M. D., 2016: Observational constraints on mixed-phase clouds imply higher climate sensitivity. *Science*, *352*(6282), 224–227. 10.1126/science.aad5300

Tatebe, H., and Coauthors, 2019: Description and basic evaluation of simulated mean state, internal variability, and climate sensitivity in MIROC6. *Geosci. Model Dev.*, *12*(7), 2727–2765. https://doi.org/10.5194/gmd-12-2727-2019

Taylor, K. E., and Coauthors, 2007: Estimating Shortwave Radiative Forcing and Response in Climate Models. *J. Clim.*, 20, 2530–2543, https://doi.org/10.1175/JCLI4143.1.

Terai, C. R., and Coauthors, 2019: Mechanisms Behind the Extratropical Stratiform Low-Cloud Optical Depth Response to Temperature in ARM Site Observations. *J. Geophys. Res. Atmos.*, *124*(4), 2127–2147. https://doi.org/10.1029/2018JD029359

Wall, C. J., 2024a: caseywall7926/Phase-Partitioned-Kernels: first release (v1.0). Zenodo. https://doi.org/10.5281/zenodo.13120941

Wall, C. J., 2024b: GCM output for Wall et al. 2024 [Data set]. Norstore. https://doi.org/10.11582/2024.00140

Wall, C. J., T. Storelvmo, J. R. Norris, and Tan, I., 2022: Observational Constraints on Southern Ocean Cloud-Phase Feedback. *J. Clim.*, 35, 5087–5102, https://doi.org/10.1175/JCLI-D-21-0812.1.

Webb, M., Senior, C., Bony, S., and Morcrette, J. J., 2001: Combining ERBE and ISCCP data to assess clouds in the Hadley Centre, ECMWF and LMD atmospheric climate models. *Clim. Dyn.*, *17*(12), 905–922. https://doi.org/10.1007/s003820100157

Zelinka, M. D., Klein, S. A., and Hartmann, D. L., 2012a: Computing and Partitioning Cloud Feedbacks Using Cloud Property Histograms. Part I: Cloud Radiative Kernels. *J. Clim.*, *25*(11), 3715–3735. https://doi.org/10.1175/JCLI-D-11-00248.1

Zelinka, M. D., Klein, S. A., and Hartmann, D. L., 2012b: Computing and partitioning cloud feedbacks using cloud property histograms. Part II: Attribution to changes in cloud amount, altitude, and optical depth. *J. Clim.*, *25*(11), 3736–3754. https://doi.org/10.1175/JCLI-D-11-00249.1

Zelinka, M. D., and Coauthors, 2013: Contributions of Different Cloud Types to Feedbacks and Rapid Adjustments in CMIP5*. *J. Clim.*, *26*(14), 5007–5027. https://doi.org/10.1175/JCLI-D-12-00555.1

Zelinka, M. D., Zhou, C., and Klein, S. A., 2016: Insights from a refined decomposition of cloud feedbacks. *Geophys. Res. Lett.*, *43*(17), 9259–9269. https://doi.org/10.1002/2016GL069917

Zelinka, M. D., and Coauthors, 2020: Causes of Higher Climate Sensitivity in CMIP6 Models. *Geophys. Res. Lett.*, *47*(1), 1–12. https://doi.org/10.1029/2019GL085782

Zhao, M., and Coauthors, 2016: Uncertainty in Model Climate Sensitivity Traced to Representations of Cumulus Precipitation Microphysics. *J. Climate*, 29, 543–560, https://doi.org/10.1175/JCLI-D-15-0191.1.

Zhao, M., 2022: An Investigation of the Effective Climate Sensitivity in GFDL's New Climate Models CM4.0 and SPEAR. *J. Clim.*, 35, 5637–5660, https://doi.org/10.1175/JCLI-D-21-0327.1.

Zhao, M., and Coauthors, 2018a: The GFDL Global Atmosphere and Land Model AM4.0/LM4.0: 1. Simulation Characteristics With Prescribed SSTs. *J. Adv. Model. Earth Syst.*, *10*(3), 691–734. https://doi.org/10.1002/2017MS001208

Zhao, M., and Coauthors, 2018b: The GFDL Global Atmosphere and Land Model AM4.0/LM4.0: 2. Model Description, Sensitivity Studies, and Tuning Strategies. *J. Adv. Model. Earth Syst.*, *10*(3), 735–769. https://doi.org/10.1002/2017MS001209

1114 Zhou, C., Liu, Y., and Wang, Q., 2022: Calculating the Climatology and Anomalies of Surface
1115 Cloud Radiative Effect Using Cloud Property Histograms and Cloud Radiative Kernels. *Adv.*
1116 *Atmos. Sci.* 39, 2124–2136. https://doi.org/10.1007/s00376-021-1166-z

1117 Zhou, C., Zelinka, M. D., Dessler, A. E., and Yang, P., 2013: An analysis of the short-term cloud
1118 feedback using MODIS data. *J. Clim.*, *26*(13), 4803–4815. https://doi.org/10.1175/JCLI-D-
1119 12-00547.1

1120 Zhu, J., and Coauthors, 2022: LGM Paleoclimate Constraints Inform Cloud Parameterizations and
1121 Equilibrium Climate Sensitivity in CESM2. *J. Adv. Model. Earth Syst.*, *14*(4),
1122 e2021MS002776. https://doi.org/10.1029/2021MS002776